EFFECT OF Ge DOPING ON Er SENSITIZATION IN THE Er DOPED Si RICH SILICA MATERIAL SYSTEM

by

FORREST R. RUHGE
B.S. University of Central Florida, 2004

A thesis submitted in partial fulfillment of the requirements
for the degree of Master of Science
in the Department of Optics
in the College of Optics and Photonics
at the University of Central Florida
Orlando, Florida

Fall Term
2006

Major Professor: Pieter G. Kik

© 2006 Forrest R. Ruhge

ABSTRACT

The continued size reduction in electronic integrated circuits has lead to a demand for on-chip high-bandwidth and low loss communication channels. Optical interconnects are considered an essential addition to the silicon electronics platform. A major challenge in the field of integrated Si photonics is the development of cost effective silicon compatible light sources. This thesis investigates the sensitization of group IV doped silica films emitting at 1.535μm for applications as silicon compatible light sources.

Thin erbium-doped silica films containing excess silicon and germanium were deposited using a multi-gun sputter system. The composition of the deposited materials was verified by Rutherford Backscattering Spectrometry. Samples from each deposition were annealed in a controlled atmosphere tube furnace at temperatures between 500ºC and 1100ºC for 30 minutes. The photoluminescence spectra from the visible to the near-infrared region were acquired while pumping either near or far from the Er^{3+} absorption lines. Under both excitation conditions all samples annealed at temperatures below 1000ºC show clear emission at 1.535μm from Er^{3+} ions in the host material. In the current literature this is attributed to exciton mediated excitation of the Er^{3+}. By contrast, in these studies indirect excitation was observed for samples annealed at temperatures well below the onset of nanocrystal nucleation and growth (between 500ºC and 1000ºC), suggesting excitation via small clusters or lattice defects. These findings could have significant implications in the further development of group IV sensitized silicon compatible gain media.

The Er^{3+} related photoluminescence was studied as a function of Ge concentration while the Si concentration was held constant. Nanocrystal related emission was observed in the visible to near-infrared region when samples containing excess group IV material were annealed at 1000ºC. An increase in the Ge concentration from 0 at.% to 3.6 at.% was found to result in an increase of the 1.535µm photoluminescence intensity by a factor two. As the Ge concentration was increased from 3.6 at.% to 12.5 at.% a gradual decrease in the Er^{3+} related photoluminescence was observed. Several samples annealed at temperatures below the temperatures required for nanocrystal formation were found to exhibit indirect Er^{3+} excitation. This observation further strengthens the conclusion that the formation of large nanocrystals is not essential for Er sensitization.

TABLE OF CONTENTS

LIST OF FIGURES vii

LIST OF TABLES xii

LIST OF ACRONYMS/ABBREVIATIONS xiii

CHAPTER ONE: INTRODUCTION 1

CHAPTER TWO: LITERATURE REVIEW 8

2.1 Rate Equations 8

2.2 Quantum Confinement 14

2.2.1 Weak Confinement Limit 17

2.2.2 Strong Confinement Limit 20

2.3 SiGe Band Gap Dependence on Composition 21

2.4 Energy Transfer From Nanocrystals to Erbium Ions 23

2.4.1 Luminescence in Porous Materials 23

2.4.2 Silicon Nanocrystals 24

2.4.3 Nanocrystal-Erbium interaction 27

2.4.4 Energy Transfer Mechanism 28

2.4.5 SiGe Nanocrystal Luminescence Properties 31

CHAPTER THREE: METHODOLOGY 33

3.1 Characterization and Modeling of the Sputter Deposition System 33

3.2 Design and Calibration of Thermal Treatment System 41

3.2 Sample Preparation 42

3.3 Compositional Analysis 44

3.4 Spectral Characterization of Er Doped Gain Media 45
CHAPTER FOUR: RESULTS AND DISCUSSION 49
4.1 Rutherford Back Scattering Results 49
4.2 Photoluminescence Characterization 51
4.3 Erbium Related Photoluminescence 55
CHAPTER FIVE: SUMMARY 72
APPENDIX A: SPECTRAL CALIBRATION OF PHOTOLUMINESCENCE SETUP 74
Calibration of the Germanium Detector 79
Calibration of the CCD Array Detector 87
APPENDIX B: RESULTS OF RBS EXPERIMENTS 98
APPENDIX C: DERIVATION OF THE EFFECTIVE Er EXCITATION CROSS SECTION 102
LIST OF REFERENCES 106

LIST OF FIGURES

Figure 1: The Stark split energy levels of the 4f shell electrons in the Er^{3+} ion. 4

Figure 2: A Schematic diagram of the three level system for Er 9

Figure 3: The energy of a quantum confined exciton in silicon as a function of nanocrystal diameter. 21

Figure 4: The excitonic band gap dependence of $Si_{1-x}Ge_x$ as a function of x as determined from low temperature photoluminescence measurements[22]. 23

Figure 5: Formation of Silicon nanocrystals by oxidization of silicon nanowires. 25

Figure 6: The AJA International sputter system used in this research. 33

Figure 7: Basic sputtering system setup. 34

Figure 8: Diagram showing the arrangement of magnets behind the target in a magnetron gun . 36

Figure 9: Relation between sputter rates and sputter powers for targets to be used in this experiment. 37

Figure 10: Flowchart showing the steps used to generate sputtering parameters from sample composition for a series of samples to be sputtered at the same time. 40

Figure 11: Calibration data and linear fit for the tube furnace 42

Figure 12: Optical system for the photoluminescence setup 46

Figure 13: Desired and actual atomic percent composition of each sample deposited for annalysys in this report.The quantities of Ar, Er and Fe are less than 1 at.%. 49

Figure 14: Detail of the desired and actual atomic percent of each sample deposited for analysis in this report. This graph shows trace quantities of iron and argon. 50

Figure 15: Visible photoluminescence spectra of sample emission when indirectly pumped with 568nm light. Nanocrystal emission is observed for the sample when annealed at 1000°C.. 52

Figure 16: Temperature dependent visible photoluminescence spectra. 53

Figure 17: Temperature dependent visible spectra of sample emission. 55

Figure 18: Typical Er spectrum of sample 04 pumped directly with 975nm laser light. 56

Figure 19: Peak Er related photoluminescence as a function of sample annealing temperature for samples of different concentrations. 57

Figure 20: Typical Er related lifetime trace of sample 04 after a 500°C anneal as well as the 568nm laser lifetime. The sample lifetime is fit with a stretched exponential function....... 58

Figure 21: Comparison of trends in Er related photoluminescence and lifetime as a function of annealing temperature for sample 04. 59

Figure 22: The active fraction as a function of annealing temperature for sample 04 ($Er_{0.43}Si_{11.58}Ge_{3.57}(SiO_2)_{28.14}$)... 63

Figure 23: Photoluminescence intensity as a function of thermal processing temperature for samples of diffrent compositions. 65

Figure 24: Excitation Spectra for Sample 04 ($Er_{0.43}Si_{11.58}Ge_{3.57}(SiO_2)_{28.14}$) for samples annealed at different temperatures as compared to the absorption spectra of erbium in a silica glass.66

Figure 25: The product of the cross-section and excitation efficiency as a function of annealing temperature for sample 04. 69

Figure 26: Comparison of the effective cross-section calculated using two different methods... 70

Figure 27: Er related photoluminescence as a function of Ge content for samples annealed at various temperatures. 71

Figure 28: Black body spectra of the calibration lamp. 75

Figure 29: Top view of the experimental setup 77

Figure 30: Oblique view of the experimental setup.. 77

Figure 31: The germanium detector.. 79

Figure 32: Czerny-Turner grating monochromator and single element detector. 79

Figure 33: Spectra of calibration lamp using the germanium detector, no long pass filter and a 300 line/mm 500nm blazed grating. The actual calibration spectrum is also plotted. This graph demonstrates the use of different resolutions to pick out finer features. 81

Figure 34: Spectra of calibration lamp using different long pass filter and a 300 line/mm 500nm blazed grating. This graph demonstrates how second order effects can be reduced by using long pass filters. 82

Figure 35: Spectra of calibration lamp using different long pass filter and a 300 line/mm 1000nm blazed grating. This graph demonstrates how second order effects can be reduced by using long pass filters. 83

Figure 36: Spectra of calibration lamp using different long pass filter and a 150 line/mm 500nm blazed grating. This graph demonstrates how second order effects can be reduced by using long pass filters. 83

Figure 37: Spectra of the calibration lamp taken with three different gratings. The actual calibration spectrum is also plotted.. 84

Figure 38: Response curve for the germanium detector using different grading. 85

Figure 39: The final response curves for the germanium detector using the three available gratings.. 86

Figure 40: The Andor 20DU401-BR-DD CCD detector. 87

Figure 41: Czerny-Turner grating monochromator and CCD array. 87

Figure 42: Spectra minus dark for the calibration source taken using the 150 l/mm 500nm blazed grating. Three spetra of diffrent regions are plotted together to cover the entire range. No long pass filter was used. 89

Figure 43: Spectra minus dark for the calibration source taken using the 300 l/mm 500nm blazed grating. Three spectra of different regions are plotted together to cover the entire range. No long pass filter was used. 89

Figure 44: Spectra minus dark for the calibration source taken using the 300 l/mm 1000nm blazed grating. Three spectra of different regions are plotted together to cover the entire range. No long pass filter was used. 90

Figure 45: Spectra of the calibration source using 150 l/mm 500nm blazed grating and different long pass filters to get an accurate representation of the spectrum...................................... 91

Figure 46: Spectra of the calibration source using 300 l/mm 500nm blazed grating and different long pass filters to get an accurate representation of the spectrum...................................... 91

Figure 47: Spectra of the calibration source using 300 l/mm 1000nm blazed grating and different long pass filters to get an accurate representation of the spectrum...................................... 92

Figure 48: Spectra that do not over lap. 93

Figure 49: Cut spectra such that there is a small gap between the tow data sets. Place both data sets together in a third data set. 93

Figure 50: Fit with a polynomial of appropriate order. 94

Figure 51: Splice the polynomial data into the third data set. 94

Figure 52: The spectra of the calibration lamp taken with the three different gratings and the CCD detector. The actual spectra of the calibration lamp is also plotted. 95

Figure 53: Response curve for the CCD array using different gratings. 96

Figure 54: Response spectra after being cropped to the useable range. 97

LIST OF TABLES

Table 1: Composition of the samples used in this study. 43

Table 2: Deposition parameters for each sample composition of interest. 43

Table 3: Composition of the samples used in this study. 51

Table 4: Coefficients for model of calibration lamp intensity. 76

LIST OF ACRONYMS/ABBREVIATIONS

PL	Photoluminescence
RBS	Rutherford Back Scattering Spectrometry
RUMP	Rutherford Universal Manipulation Program
LED	Light Emitting Diode
FWHM	Full Width at Half Maximum
RF	Radio Frequency
AOM	Acousto-Optic Modulator
CCD	Charge Coupled Device
PMT	Photo Multiplier Tube
DC	Direct Current
HV	High Voltage
GND	Ground
NIR	Near Infrared
VIS	Visible

CHAPTER ONE: INTRODUCTION

Over the past decade, dramatic changes have occurred in telecommunications, where glass fiber based optical interconnects are rapidly replacing traditional copper conductors. These changes were driven by increasing demand for high speed Internet and other high throughput communications in the residential sector and have stimulated interest in large bandwidth fiber to home systems[1]. An analogous transformation is occurring on a much smaller length scale in electronics. Continued miniaturization of integrated silicon electronics for use in the personal computer market have reached a point where fundamental laws of physics are beginning to pose problems, and as a result the silicon electronics industry is currently investing heavily in the development of optical on-chip communication channels. [2]. One of the key problems is thermal management: traditional copper-based interconnects produce significant resistive heating, posing an ever greater challenge due to the steady increase in interconnect densities on computer chips. A second challenge is formed by the data transfer bandwidth required: as processing power of central processing units (CPUs) increases, larger volumes of data need to be transported across the chip. In copper interconnect technology, electrical resistivity and capacitance limit the maximum data rate. A final problem is formed by clock synchronization. As the clock speed of CPUs increases to several GHz, the time delay incurred by a signal as it is passed between several on chip components becomes substantial, resulting in synchronization problems. For this reason current technology includes delay compensation circuits that take away from the available silicon 'real estate' (area available to electronics circuits). These three problems could be mitigated by switching to optical on-chip interconnects, as they enable large bandwidth (THz range), low loss and consequently negligible resistive heating, and fast signal

speeds resulting in reduced signal delays[3]. A cost effective optical interconnect solution would require the lithographic definition of optical components directly on silicon, as opposed to aligning and attaching external optical device elements onto the chip [3]. Chief requirements for on-chip optical communications components are affordable optical components that can be used for light generation, transmission, modulation, amplification, and detection. Already, silicon compatible waveguides modulators and detectors operating at telecommunications wavelengths have been demonstrated [4-6]. However, an effective silicon based light source is still lacking.

The most natural choice for developing a silicon compatible light source would be to use the Si itself as the light emitter. Obtaining photon emission from silicon is difficult due to the fact that silicon is an indirect band gap semiconductor. In indirect semiconductors, the electrons and holes that make-up the excitons do not possess the same momentum. Since photons do not carry sufficient momentum to make up for this difference, exciton recombination in silicon requires that the momentum difference is overcome by the excitation or absorption of phonons. This results in a competition between two main recombination pathways: non-radiative and radiative recombination. Radiative recombination requires the simultaneous emission of a photon and absorption or emission of one or multiple phonons. This represents a multi-body recombination process with a low probability and corresponding long lifetimes on the order of several μs at room temperature. For that reason, in bulk silicon non-radiative deep-level recombination dominates over radiative recombination. In deep level recombination, a free carrier is trapped in the Coulomb potential of an attractive center in the Si lattice (at a lattice defect site or at a chemical impurity), where it subsequently gradually releases phonons as it becomes more and more tightly bound. This is followed by a similar capture of a carrier of the opposite polarity,

completing the recombination process. In this process, the momentum difference can be overcome via a sequence of single phonon emission events. This makes the nonradiative process more likely than the ‘multi-body’ radiative recombination, causing indirect semiconductors such as silicon to be inefficient emitters [7-9].

Due to the inefficient light emission from silicon, several alternative approaches are being considered [4, 5]. One approach focuses on the development of silicon based sources that are compatible with the standard telecommunications wavelength of 1.54 µm. First, this would allow for direct integration of telecommunication systems with silicon photonics. Secondly, light with a wavelength of 1.54 µm is not absorbed by silicon, allowing the use of silicon itself as a high index, high confinement optical waveguide.

The widespread use of 1.5 µm light for data transport is related to the telecommunication industry. This wavelength coincides with the lowest loss of traditional glass fiber, and is therefore ideal for and long-range communications [10]. Erbium is often used for generation and amplification of the 1.5 µm telecommunication wavelength. When erbium is incorporated into an oxide matrix it generally assumes the trivalent Er^{3+} configuration. In this triply ionized state, the erbium ion exhibits distinct energy levels due to different allowed electronic configurations of the 11 electrons present in the 4f shell of the Er ion. Figure 1 shows the corresponding energy levels of the Er^{3+} ion. Arrows represent the transition made when the ion is optically pumped in the second excited state (Green Up Arrow), followed by non-radiative decay from the second excited state to the first excited state (Blue Dotted Down Arrow) and radiative decay from the first excited state to the ground state (Blue Solid Down Arrow).

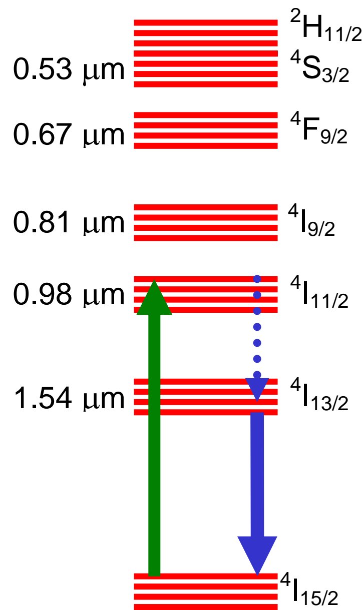

Figure 1: The Stark split energy levels of the 4f shell electrons in the Er^{3+} ion.

Spin-spin and spin-orbit coupling within the 4f shell results in energy levels that are generally separated by hundreds of meV. Inside amorphous host materials, each of these levels is Stark-split into a manifold with a typical width of tens of meV. The two lowest lying energy states are separated by 0.8 eV, resulting in a possible radiative transition of the ion from its first excited state ($^4I_{13/2}$) to the ground state ($^4I_{15/2}$) producing photons with a wavelength of ~1.54μm. The spectral line shape is defined by the Stark splitting induced by the host, and the width is affected by thermal redistribution over the available energy levels in the manifold. The emission at 1.54μm from the Er^{3+} ion makes erbium an excellent emitter for use in fiber communications applications.

While erbium is a good emitter of 1.54μm light, it requires large pump powers to obtain population inversion for gain. This is a result of the quantum mechanical nature of the energy

levels. Optical intra-4f transitions are parity forbidden, but can become weakly allowed due to the influence of a non-centrosymmetric host material. This leads to finite but extremely small absorption and emission cross-sections, on the order of $10^{-21}cm^3$ [11]. The small absorption cross-section of the Er ions necessitates high pump powers and narrowband optical excitation sources to excite the Er ions, preventing the cost effective integration of Er based light sources on silicon. A solution to this problem is to *sensitize* the Er ions. This involves the use of an optical dopant with a large absorption cross-section, that can subsequently transfer the absorbed energy to the Er ions. A traditional sensitizer for Er^{3+} absorption is the Ytterbium ion (Yb^{3+}), a rare earth with a broad absorption band around 980nm. A more recent development is the use of semiconductor nanocrystals as sensitizers, combining silicon compatible materials processing with large absorption cross-sections and efficient energy transfer. This type of material could results in the development of a silicon laser pumped by a low cost broad-band excitation source such as a Light Emitting Diode (LED).

Recently, a large amount of research has been conducted on nanocrystalline silicon as a sensitizer for erbium doped silica (SiO_2). Silicon nanocrystals exhibit a broad absorption spectrum, due to the existence of extended energy bands in silicon. The cross-section for absorption of light by silicon nanocrystals with a mean radius of ~1.7 nm is on the order of $10^{-16}cm^2$ [12]. This is significantly higher than that of erbium ($10^{-21}cm^2$).

In order to make use of the large absorption cross-section of the silicon nanocrystals and the emission of the erbium at 1.5 μm, erbium has been incorporated into a thin silica films containing significant concentrations of excess silicon (typical composition $Si_{40}O_{60}$, equivalent to

$Si_{10}(SiO_2)_{90}$. When thermally annealed at temperatures above 1000°C these films have been shown to contain silicon nanocrystals. Such Er and Si nanocrystal doped samples were found to exhibit strongly enhanced erbium luminescence as well as a broad visible emission feature attributed to radiative recombination of bound electron hole pairs (excitons) inside silicon nanocrystals. It was found that the incorporation of higher Er concentrations into the host material results in a reduced silicon nanocrystal luminescence intensity [13, 14] suggesting that an energy transfer takes place from the excitons in the nanocrystals to the Er ions in the host material. This interpretation was further corroborated by the demonstration of virtually identical excitation spectra of the nanocrystal based emission and the Er related emission[15]. It has been demonstrated via several different methods that the incorporation of silicon nanocrystals in silica films can enhance the effective erbium absorption cross-section by two orders of magnitude[15]. By combining the large absorption cross-section of Si nanocrystals with the narrow band emission of erbium, a low power broad band pumped erbium based amplifier or laser operating at 1.5 μm could be developed.

In order to optimize the performance of nanocrystal sensitized gain media, the details of the nanocrystal-Er interaction need to be understood. In particular, the development of nanocrystal sensitized amplifiers and lasers requires the presence of high concentrations of nanocrystals and high concentrations of active erbium, conditions which are difficult to achieve simultaneously. The research in this thesis investigates the effect of the nanocrystal composition and size on the energy transfer process. In order to study the role of nanocrystals, photoluminescence studies will are performed on samples processed at different annealing temperatures. Secondly, in order

to study the effect of the nanocrystal band gap, the nanocrystal composition is changed from pure Si to a Si_xGe_{1-x} compound with varying Si concentration.

CHAPTER TWO: LITERATURE REVIEW

The understanding of the observations in this research project requires knowledge of three main concepts: rate equations, quantum confinement and energy transfer. The sections below discuss these fundamental concepts in more detail.

2.1 Rate Equations

Although the exact microscopic mechanism underlying the energy transfer between silicon nanocrystals and erbium is not well understood, it is possible to model the observed trends in the optical measurements in terms of the excitation and recombination of quantum confined excitons (bound electron hole pairs) in the Si nanocrystals, and a phenomenological energy transfer probability from the excitons to the Er ions. The optical properties of the Er ions are described by a rate equation model involving spontaneous and induced transitions between the 4f energy levels.

Rate equations are used to describe physical processes in terms of probabilities of making transitions between distinguishable physical states of the system. In most cases, it is found that the rate of change of a quantity is related its value. The simplest form of a rate equation is shown in Equation 1.

$$\frac{dN}{dt} = AN \qquad (1)$$

Here N represents for example the number of atoms in a certain state, which they leave with a typical rate given by A, where A has units s^{-1}. Equations of this form are used to describe many different phenomena including half lives, chemical reaction equilibrium, and laser gain. In this work we will use the rate equation approach to model physical processes in the developed thin film gain material.

Rate equations may be used to describe several optical phenomena, including optical absorption, spontaneous emission, and stimulated emission. These equations will be used to model the nanocrystal and Er luminescence intensities and lifetimes.

Er^{3+} ions can under certain conditions be described as a three level system as sketched in Figure 2. In this type of system a population of atoms may be in one of the excited states or in the ground state. The number of atoms in the first excited state is denoted N_1, the number of atoms in the second excited state is denoted N_2, and the number of atoms in the ground state N_0. The total number of atoms in the system will be $N_T=N_0+N_1+N_2$.

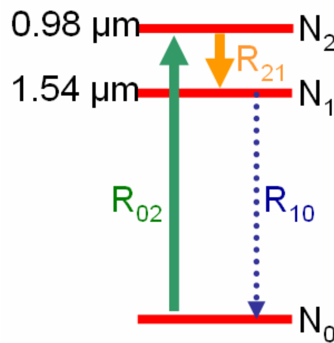

Figure 2: A Schematic diagram of the three level system for Er

Initially we will assume that all of the atoms are in the ground state. If there is an incident photon with energy equal to the difference in energy of the ground state and the second excited state then an atom may be promoted to the second excited state. This process of absorption can be described by:

$$\frac{dN_2}{dt} = B_{01}\rho(\nu)N_0 \qquad 2$$

In this equation we see that the rate of change in the number of atoms in the second excited state is proportional to the number of atoms in the ground state. The proportionality constant is given by the Einstein coefficient for absorption (B_{01}) and the electromagnetic spectral energy flux ($\rho(\upsilon)$). In the case where the system is illuminated with monochromatic light of frequency υ Equation 2 one may be written as follows (Equation 3).

$$\frac{dN_2}{dt} = \sigma_{02}(\nu)\frac{I_\nu}{h\nu}N_0 \qquad 3$$

In Equation 3 σ_{02} is the cross-section for a transition from the ground state to the second excited state (i.e. absorption) and the quantity $I_\upsilon/(h\upsilon)$ is the incident photon flux. In this work the cross-section and incident photon flux will often be grouped together in one term which will be referred to as the pump rate (Equation 4).

$$R_{ij} = \sigma_{ij}\frac{I_\nu}{h\nu} \qquad 4$$

Where the quantities i and j representing the initial and final energy levels.

A second process that is observed in the diagram shown in Figure 2 is the decay of the ion from level 2 to level 1. This decay process could occur non-radiatively or radiatively, which is modeled with a single effective decay rate R_{21}. This effective decay rate is generally described by the *lifetime* of the level, denoted τ_1 (units s^{-1}) as shown in Equation 5.

$$R_{10} = \frac{1}{\tau_1} \qquad 5$$

Radiative relaxation directly to the ground state is also possible; however in Er^{3+} this type of relaxation forms a negligible contribution to the total decay rate. A third process that can occur is stimulated emission, which can give rise to gain. Stimulated emission from level 1 to the ground state scales with the electromagnetic spectral energy density ($\rho(\upsilon)$) and the Einstein coefficient B_{10} as seen in equation 6.

$$\frac{dN_1}{dt} = -N_1 B_{10} \rho(\nu) \qquad 6$$

When the system is illuminated with monochromatic light this equation simplifies to:

$$\frac{dN_1}{dt} = -N_1 \sigma_{10}(\nu) \frac{I_\nu}{h\nu} \qquad 7$$

Again, it is convenient to refer to the cross-section times the incident photon flux as the spontaneous emission rate (R_{10}). The resulting rate equation with this substitution is:

$$\frac{dN_1}{dt} = -N_1 R_{10} \qquad 8$$

Although the materials used in this study are intended as gain media, stimulated emission does not play a significant role in the presented photoluminescence studies due to the low pump powers used, the small sample thickness and the small Er cross-sections, as discussed above.

Ignoring stimulated emission, the above rates may be combined to describe the population in each of the energy levels. The equations that describe the three level system shown in Figure 2 are presented below.

$$\frac{dN_2}{dt} = N_0 R_{02} - N_2 R_{21} \qquad 9$$

$$\frac{dN_1}{dt} = N_2 R_{21} - N_1 R_{10} \qquad 10$$

$$\frac{dN_0}{dt} = -N_0 R_{02} + N_1 R_{10} \qquad 11$$

$$N_T = N_0 + N_1 + N_2 \qquad 12$$

For higher order systems (systems with more than three levels) there will be a rate equation for each level describing the population changes of each level. One of the three time dependent

equations can be eliminated by realizing that the total number of atoms in the system is constant (Equation 12). This system of rate equations can be solved analytically for the steady state (*dN/dt*=0) populations of each level. The time dependent solutions can be easily solved in simple systems, but as more mechanisms and levels are included the solutions become more complicated, requiring numerical approaches.

When modeling Er with the system shown in Figure 2 non-radiative relaxation can be assumed to be fast compared to the pump rate and the radiative decay rate since the lifetime τ_2 of level 2 is typically of the order of 10 μs, while the lifetime of the first excited state is of the order of 1-10 ms. At pump rates significantly less than $1/\tau_2$, the population in the second excited state can be assumed to be approximately zero. This modifies the rate equations to those of a quasi-two level system, in which stimulated emission from level 2 is neglected. In this case, the effective pump rate at which level 1 is populated is thus given by R_{02}, resulting in the following equation for the population in N_1.

$$\frac{dN_1}{dt} = R_{02}N_0 - N_1/\tau_1 \qquad 13$$

In steady state Equation 13 becomes Equation 14.

$$0 = R_{02}N_0 - N_1/\tau_1 \qquad 14$$

By using Equation 5, Equation 14 can be written as Equation 15.

$$R_{02}N_0 = \frac{1}{\tau_1}N_1 \qquad 15$$

Using $N_T = N_1+N_2$, and defining $\tau = \tau_1$ for simplicity, Equation 15 becomes Equation 16.

$$N_1 = N_T \frac{R_{02}\tau}{1+R_{02}\tau} \qquad 16$$

At low pump powers, where the product $R_{02}\tau$ is small, the denominator is approximately equal to 1, resulting in $N_1 = N_T R_{02}\tau$. Writing R_{02} in terms of the photon flux Equation 17 is obtained.

$$N_1 = \sigma_{02}(\nu)\frac{I_\nu}{h\nu}\frac{N_T}{\tau} \qquad 17$$

Since the photoluminescence (PL) intensity is linearly proportional to N_1, Equation 17 describes the observed trends in Er emission intensities in low power PL measurements. This allows us to extract relative values for the effective absorption cross-section.

2.2 Quantum Confinement

According to quantum mechanics, electrons inside solids need to be described by probability waves known as wavefunctions that determine the location, the energy and the momentum of the electrons. In this quantum mechanical picture, electrons with a long wavelength have a low kinetic energy while those with a short wavelength have a large kinetic energy. Quantum

confinement is an effect that appears when the physical size of the semiconductor becomes comparable to the electron wavelength. In nanoscale semiconductor particles, electron reflections at the semiconductor surface put a constraint on the minimum electron wavelength and thus the minimum electron energy. As a result, the confinement of an exciton within the physical boundaries of a nanoscale semiconductor crystal or 'nanocrystal' results in a shift of the electron energy levels and an effective increase in the difference in energy between the semiconductor conduction and valence band, known as the semiconductor band gap. Optical excitation of electrons into the conduction band generates electron hole (e-h) pairs in the nanocrystals. Due to the opposite charge of electrons and holes, bound states e-h states can exist, called excitons. These excitons are charge neutral and can move through the semiconductor volume. The Coulomb attraction between the electron and hole causes the apparent energy gap observed in absorption and emission from semiconductors to be smaller than the energy required for the generation or recombination of a free electron and hole. The amount of confinement of such excitons is often expressed in terms of the size of an unconfined exciton, known as the Bohr radius. The Bohr radius of an exciton in bulk silicon is 4.3nm [16]. As the dimensions of the semiconductor approach the size of the Bohr radius of the exciton, the center of mass motion of the exciton is confined to a small volume and the system is described as weakly confined. As the dimensions become smaller than the exciton Bohr radius the location of the electron and the hole are no longer dominated by their mutual Coulomb interaction, but instead are dictated by the presence of the nanocrystals surface (or more precisely the nanocrystal-matrix interface). In this situation, the system is described as being *strongly confined.* This confinement results in an further increase of the band gap energy and making a indirect band gap "quasi direct" [17]. The following steps follow the analysis used in Gaponenko [16].

The allowed energy states of quantum confined excitons can be calculated from the two body Schrödinger equation using the effective mass (m*) of the electron and hole (Equation 18).

$$-\frac{\hbar^2}{2m_e^*}\nabla_e^2\psi(x)-\frac{\hbar^2}{2m_h^*}\nabla_h^2\psi(x)-\frac{e^2}{\varepsilon\left|r_e-r_h\right|}\psi(x)=E\psi(x) \qquad 18$$

This equation can be shown to require a minimum radius of the exciton called the exciton Bohr radius (a_B). It also predicts the exciton Rydberg energy (Ry^*) which is the energy difference between unbound and bound electron hole pairs (Equations 19 and 20).

$$a_B=\frac{\varepsilon_0\varepsilon_r\hbar^2}{\mu e^2} \qquad 19$$

$$Ry^*=\frac{e^2}{2\varepsilon_0\varepsilon_r a_B} \qquad 20$$

In Equation 19, μ is the effective mass of the system given by Equation 21.

$$\mu=\left(m_e^{*-1}+m_h^{*-1}\right)^{-1} \qquad 21$$

The energy (E_n) of excitons in semiconductor materials is given by the band gap energy minus the exciton binding energy (Equation 22).

$$E_n = E_g - \frac{Ry^*}{n^2} \quad 22$$

Thus, luminescence arising from exciton recombination occurs at energies just slightly below the band gap of the host material.

In the current treatment excitons in nanocrystals are modeled with the effective mass approximation. This approach assumes that the effective mass of the electron and hole are not affected by the finite size of the nanocrystal. It also assumes that the nanocrystals can be modeled as a spherical volume with boundaries that are represented by an infinite potential barrier. For comparison, in the experiments group IV nanocrystals are embedded in an amorphous oxide matrix with a band gap exceeding 8eV.

The modeling of quantum confinement is most easily described in two limiting cases. When the nanocrystal size is several times the exciton Bohr radius, the system is considered to be in the weak confinement limit. When the nanocrystal size is much smaller than the Bohr radius the system is considered to be in the strong confinement limit.

2.2.1 Weak Confinement Limit

In the weak confinement limit the nanocrystal radius is several times larger than the exciton Bohr radius. In this limit the effects from the electron and hole effective mass, the center of mass motion of the exciton, and the dielectric screening of the host material are included. In this case the confinement energy is dominated by the confinement of the center of mass of the exciton.

The time independent Schrödinger equation that describes the exciton in a spherical volume having infinite potential barriers is given by Equation 23[16].

$$-\frac{\hbar}{2M}\nabla^2\psi(r,\theta,\varphi) = E\psi(r,\theta,\varphi) \qquad 23$$

Where M in Equation 23 is the exciton mass. The Laplacian in spherical coordinates is given by Equation 24.

$$\nabla^2 = \frac{\partial}{\partial r}\left(r^2\frac{\partial}{\partial r}\right) \qquad 24$$

The solutions to Equation 23 are functions called spherical harmonics, describing the angular probability distribution functions in terms of the orbital quantum number l and the magnetic quantum number m. The corresponding energy levels of the weakly confined exciton are described by Equation 25.

$$E_{ml} = \frac{\hbar^2\chi_{ml}^2}{2Ma^2} \qquad 25$$

In this equation χ_{ml} represent the zeros of the Bessel Functions and M is the total mass of the electron hole pair. The above result shows that the energy of the exciton increases as the radius of the potential well decreases. If this term is added to the energy of the exciton in a

semiconductor, the total energy of the exciton in a semiconductor nanocrystal can be found (Equation 26).

$$E_{nml} = E_g - \frac{Ry^*}{n^2} + \frac{\hbar^2 \chi_{ml}^2}{2Ma} \qquad 26$$

It is customary to label the angular distributions of the exciton center of mass motion in capital letters (1S, 2S, 2P, 3S…) and the internal states of the exciton with lower case letters(1s, 2s, 2p, 3s…). Given that $\chi_{m0} = m\pi$ it is clear that the lowest energy that a confined exciton can have corresponds to m=1, resulting in Equation 27.

$$E_{1S1s} = E_g - Ry^* + \frac{\hbar^2 \pi^2}{2Ma} \qquad 27$$

The last term may be written in terms of the exciton Bohr radius as shown in Equation 28.

$$E_{1S1s} = E_g - Ry^* \left(1 - \frac{\mu}{M}\left(\frac{\pi a_B}{a}\right)^2\right) \qquad 28$$

In indirect semiconductors, these optical transitions occur on a microsecond time scale. In our experiments, highly excited e-h pairs are generated, that rapidly (ps timescale) relax to thermal equilibrium, resulting in emission from predominantly the lowest energy exciton state. It should be noted that for small nanocrystals, the exciton recombination is thought to be occurring via

oxygen related surface states, resulting in a relatively size-independent low emission energy[18, 19].

2.2.2 Strong Confinement Limit

The strong confinement limit describes the situation where the size of the nanocrystal is significantly smaller than the exciton Bohr radius of the exciton. In this case the spatial distribution of the electron and hole wave functions becomes dominated by the boundary conditions, resulting in significant wave function overlap. To first order approximation, the energy of a strongly confined exciton is thus given by the bandgap plus the sum of the confined electron and hole energy. Ignoring the Coulomb interaction this gives rise to the following energy levels (Equation 29).

$$E_{ml} = E_g + \frac{\hbar^2 \chi_{ml}^2}{2m_e^* a} + \frac{\hbar^2 \chi_{ml}^2}{2m_h^* a} = E_g + \frac{\hbar^2 \chi_{ml}^2}{2\mu a} \qquad 29$$

A more accurate solution needs to account for the effects of the Coulomb interaction in the presence of a confining potential $U(r)$ (Equation 30).

$$E\psi = -\frac{\hbar^2}{2m_e}\nabla_e^2 \psi(r,\theta,\varphi) - \frac{\hbar^2}{2m_e}\nabla_h^2 \psi(r,\theta,\varphi) - \frac{e^2}{\varepsilon |r_e - r_h|} + U(r) \qquad 30$$

The exciton energy in the strong confinement limit has been calculated to be approximately given by Equation 31 [16, 20].

$$E_{1S1s} = E_g + \left(\frac{a_B}{a}\right)^2 Ry^* \left[\pi^2 - 1.786\frac{a}{a_B} - 0.248\left(\frac{a}{a_B}\right)^2\right] \quad 31$$

The size dependence of the first energy state of the exciton as a function of nanocrystal radius is plotted in Figure 3.

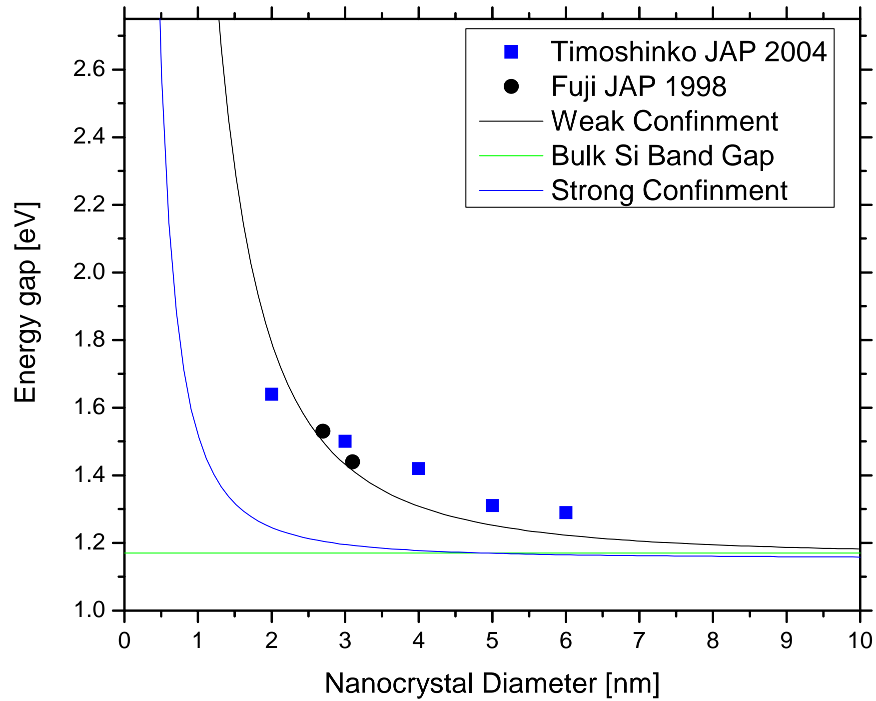

Figure 3: The energy of a quantum confined exciton in silicon as a function of nanocrystal diameter

2.3 SiGe Band Gap Dependence on Composition

The research in this thesis investigates energy transfer between group IV nanocrystals and Er^{3+} ions. When using pure Si nanocrystals it has been found that the Er excitation rate is a function of the size of the nanocrystal and consequently the nanocrystal band gap[21]. Studies show that a

smaller nanocrystal size results in a higher Er PL intensity [21]. In the present study, $Si_{1-x}Ge_x$ composites are used as an second method of controlling the nanocrystal band gap. The ability to tune the nanocrystal band gap by material composition in principle allows for independent investigation of the effects of nanocrystal band gap and size. These types of investigations could answer questions about the nanocrystal to Er energy transfer mechanism.

In order to fabricate nanocrystals of the same size with different band gaps, or nanocrystals of different sizes with the same band gap, the dependence of the band gap on composition must be known. The compositional dependence of the band gap in the SiGe system has been studied numerically and experimentally [22] and a fit of the experimental data are presented in Figure 4. Note that these data represent bulk composites, i.e. not including any quantum confinement. Also note that these values represent the band gap energy at low temperature (T=2.4 K).

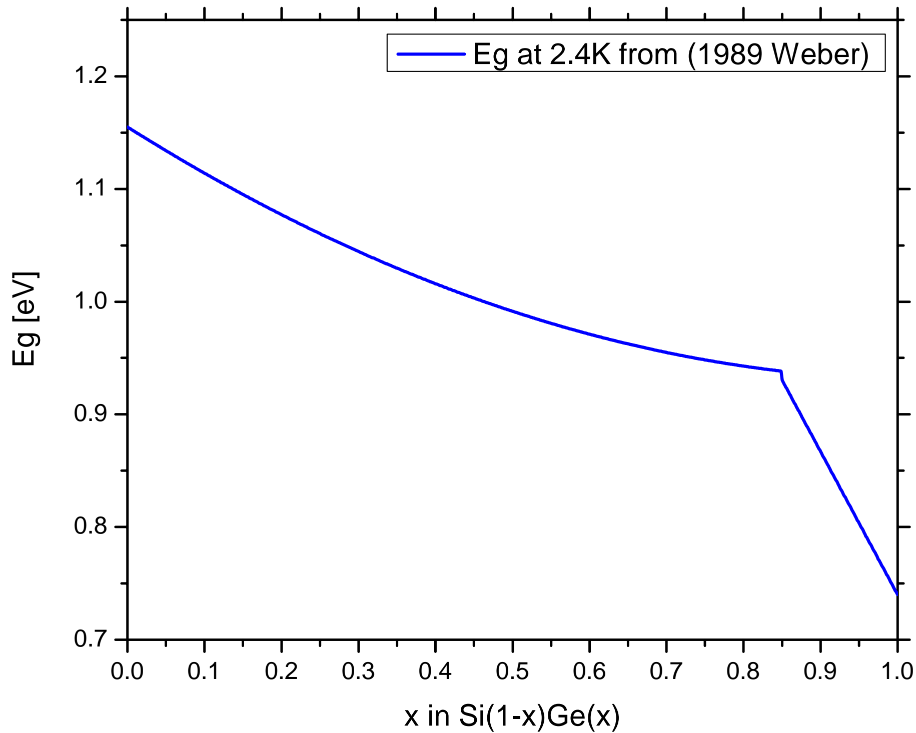

Figure 4: The excitonic band gap dependence of $Si_{1-x}Ge_x$ as a function of x as determined from low temperature photoluminescence measurements[22].

2.4 Energy Transfer From Nanocrystals to Erbium Ions

2.4.1 Luminescence in Porous Materials

Porous silicon was first considered as a novel method for use as an isolation dielectric in integrated circuits because of its low conductivity [23]. The first demonstration of light emission in porous silicon occurred in 1990 [9]. Silicon wafers were electrochemically etched in HF to cause the formation of micro-pores whose diameter and depth depended on the substrate resistivity and anodization conditions. When these samples were illuminated with green or blue

light it was found that they emitted red light. Photoluminescence spectroscopy experiments on these samples revealed that the luminescence shifts to higher energy and becomes more intense as the porosity in the samples increases. The observed effects were attributed to two dimensional quantum confinement (i.e. electron motion is inhibited in 2 directions, resulting in quasi one-dimensional wave functions) which correctly predicts both luminescence from energies higher than the bulk band gap of the semiconductor and an increase in the luminescence intensity as the confinement increases.

Shortly after this discovery, several other groups demonstrated luminescence in many different kinds of porous materials. In 1991 Gardelis et al. published the first record of photoluminescence from porous $Si_{0.85}Ge_{0.15}$ and compared it with that of porous Si. It was found that both the porous Si and SiGe display a broad photoluminescence spectrum spanning from the near IR to the visible region at 12K[8]. It is also noted that the emission peak of the SiGe occurs at lower energy than that of the Si, due to the lower band gap of the SiGe compound compared to Si [8]. The results were also found to be consistent with the 2D quantum confinement model, showing increased emission energy as the porosity increased [8].

2.4.2 Silicon Nanocrystals

Structural investigation of porous silicon samples revealed that the electrochemical etch produces thin wires of silicon, the surface of which subsequently oxidizes to create a silica coating on the outside of the wires. The oxidation of silicon is a self limited process that affects only the first few nanometers from the surface. The silicon structures in porous silicon are not of

uniform thickness and their diameters vary as a function of depth into the sample. Therefore the oxidation of the wires results in both narrow regions that have a higher effective band gap or that oxidize completely, as well as thicker portions that have a well defined Si core and a thin SiO_2 coating. As a result the Si core is effectively broken up into separate crystalline regions, as schematically indicated in Figure 5 [24].

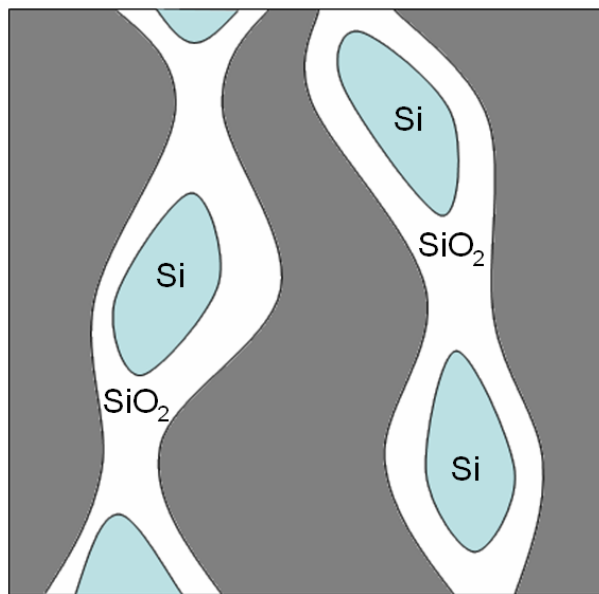

Figure 5: Formation of Silicon nanocrystals by oxidization of silicon nanowires.

The nano-scale crystalline regions of Si in these structures were termed silicon nanocrystals. The formation of these nanocrystals results in the quantum confinement of excitons, giving rise to bright high energy (red) emission from silicon.

Once it was realized that nanocrystals were chiefly responsible for luminescence in silicon, new ways of creating silicon nanocrystals in silica were investigated. Several different methods make use of silicon rich silica films, formed for example by ion implantation or co-sputtering. These films are then annealed in an inert gas or in forming gas (a mixture of a few percent of H_2 in N_2)

atmosphere. At temperatures above 1000°C the excess silicon becomes mobile, initially resulting in the formation of small nuclei of a few Si atoms, followed by the growth of larger Si crystallites using the available excess silicon[25, 26]. Hydrogen is used to passivate the Si-SiO_2 interface. In this process, non-saturated bonds, or 'dangling bonds' (available valence electrons, e.g. on a 'trivalent Si atom' bound to only three neighboring atoms) are occupied by a H atom, resulting in a reduction of the number of deep electronic levels at the Si-SiO_2 interface, and improving the exciton emission efficiency[27, 28]. The solid state growth of nanocrystals results in a broad distribution of nanocrystal sizes, giving rise to a broad emission band due to varying degrees of quantum confinement. A relatively new method of silicon nanocrystal fabrication that allows for improved control over the nanocrystal size was implemented by Timoshenko. In this method films were prepared by reactive evaporation of SiO powder, while alternating the oxygen background pressure during evaporation. This results in multilayers of silicon rich silica embedded between silica layers. Subsequent annealing of these samples causes the formation nanocrystals with an improved the size distribution of nanocrystals [21]. Although similar samples could in principle be fabricated at UCF, this approach was not attempted here.

The luminescence characteristics of silicon nanocrystals have been extensively studied. It is commonly observed that silicon nanocrystal related luminescence is characterized by broad spectra centered around $\lambda \approx 800$nm with a full width half max (FWHM) of approximately 100-200nm [28]. Studies have found that the luminescence peak blue shifts with a decrease in size of the nanocrystal [13, 21], in correspondence with the quantum confinement model. For nanocrystals with a diameter of 2±0.5nm the center of the peak luminescence can be observed at 1.5eV [21], 0.4eV higher than the bulk band gap of silicon. In addition to this effect, studies by

Imakita have shown that the band structure of the silicon nanocrystals changes as the nanocrystal diameter decreases [29]. These studies conclude that while nanocrystals with a diameter of 5.8nm still predominantly exhibit the band structure of bulk silicon, nanocrystals with a diameter of 3.4nm show a quasi direct band gap. The formation of the quasi direct band gap in nanocrystals eases the momentum-conservation requirement allowing for more efficient light emission from these structures for materials that have an indirect bulk bandgap. This results in a higher emission efficiency as the diameter is decreased. Experimentally it has been observed that the photoluminescence intensity of silicon nanocrystals is approximately inversely proportional to the nanocrystal diameter [14, 29].

2.4.3 Nanocrystal-Erbium interaction

After the first studies revealing light emission from porous silicon, it appeared that efficient emitters could be generated in silicon. However, it was demonstrated that the Si bandgap retains its indirect character even for significantly confined systems (confinement energy ~1 eV). This implies a persistent weak oscillator strength for radiative transitions. As a result, free carrier absorption will dominate over stimulated emission by excitons, making lasing from excitons in spherical ideally passivated Si nanocrystals impossible. In parallel with these efforts, significant research had been done on obtaining light emission from silicon by directly including Er ions into the Si matrix. It was found that Er can be excited by excitons in the silicon matrix, resulting in 1.54 μm emission from silicon. Although this discovery initially generated great interest, it was found that this process work efficiently only at low temperatures (< ~100K) due to a process

called energy backtransfer. In this process, an excited Er ion de-excites while generating an exciton[30].

An combined approach using Er ions in combination with nanocrystals was found to solve this problem. In 1997 Fuji incorporated different concentrations of erbium into the silicon rich silica system by radio frequency (RF) magnetron co-sputtering. These samples were then annealed and their photoluminescence properties studied. It was conclusively shown that as the erbium concentration was increased the silicon nanocrystal related luminescence was quenched and the erbium related luminescence at 1.5μm was increased dramatically [13]. These studies provided evidence that energy is transferred from the silicon nanocrystals to the erbium ions. In subsequent work it was shown that silicon nanocrystals can be used to pump not only erbium but also other rare earth ions [15]. Other demonstrations of the coupling of energy from silicon nanocrystals to erbium ions showed that the effective erbium cross-section is enhanced by up to four orders of magnitude [15, 31]. Nanocrystal size dependent studies showed that smaller nanocrystals produce faster energy transfer [21].

2.4.4 Energy Transfer Mechanism

A main concern in determining the energy transfer mechanism is determining where the erbium ions are located. The erbium ions can potentially be located in the silicon nanocrystal, the silica matrix, or at the silicon/silica interface. Investigation of this topic by Franzò indicates that the erbium ions are located predominantly in the silica matrix around the nanocrystals [15, 32]. The spectral shape of the emission around 1.5μm is influenced by the Stark splitting of the energy

levels in the 4f shell of the erbium ion. This Stark splitting is strongly influenced by the crystal field around the ion. Thus if the erbium ions were incorporated in a silicon nanocrystal with a well defined crystalline order, the line shape of the luminescence would exhibit sharp peaks. In Franzò's experiments the luminescent line shape most resembles that of erbium in silica. This is consistent with the fact that the solubility of erbium in silicon is much less than that of erbium in silica. It is now commonly accepted that the erbium ions reside in the silica matrix around the nanocrystals.

As research on the energy transfer mechanism progressed, an apparent inconsistency between the characteristic behavior of the exciton photoluminescence lifetime and intensity was observed [15]. Initially it was thought that the reduction of the nanocrystal related luminescence at 0.8eV in the presence of Er was due to a competition between radiative recombination of quantum confined excitons in the nanocrystal, and energy transfer to Er ions. The lifetime of the nanocrystal luminescence was thus expected to be affected by the Er concentration, since an increase in the erbium concentration would increase the energy transfer rate from the nanocrystal, reducing the exciton lifetime and emission intensity. This correlation was not observed in experiments by Franzò [15]. In her observations the nanocrystal lifetime was found to be independent of the erbium concentration. To explain this Franzò proposed that the nanocrystal luminescence did not come directly from the quantum confined exciton levels but from luminescent centers associated with defects in the nanocrystal [15].

An alternative explanation for the behavior found by Franzò was offered by Kik. In the proposed model the energy transfer rate is assumed to be significantly faster than the typical radiative

recombination rate of the excitons. In this case, the presence of an erbium in the immediate environment of the nanocrystal results in a energy transfer that is sufficiently fast to render the nanocrystal effectively 'dark' [11]. Any remaining nanocrystals that do not interact with erbium ions will exhibit the characteristic nanocrystal lifetime. As the erbium concentration is increased, the probability of having an erbium ion near the nanocrystal surface increases, and as a result the photoluminescence intensity decreases. Thus the nanocrystal luminescence lifetime may be largely unaltered even though the photoluminescence intensity is found to decrease.

An important characteristic of the energy transfer mechanism is its speed, i.e. the typical time constant associated with the energy transfer process, since it will set an upper limit to the rate at which the Er ions can be excited, resulting in a limit on the output power. Several studies have investigated the transfer rate. The first publication on this topic put an lower limit on the energy transfer rate on the order of 10^6 s^{-1} [11]. A subsequent study by Watanabe showed that the energy transfer for smaller nanocrystals is faster than the energy transfer from large nanocrystals. Their measurements showed that the energy transfer time for nanocrystals of 5.5nm mean diameter was 115µs while the transfer from 2.7nm nanocrystals occurred in 11µs [33]. These slow transfer times suggest that the energy transfer is not mediated by photons.

Several mechanisms have been proposed for the energy transfer phenomenon. As mentioned above, it is unlikely that photons play a role in the energy transfer mechanism [11, 32, 33]. It is also commonly accepted that quantum confined excitons are crucial to the energy transfer mechanism [31, 33]. Evidence has been presented that phonon assisted energy transfer may play a role, although this is not considered to be the main erbium excitation mechanism [21, 33].

Resonant energy transfer has also been demonstrated when the silicon nanocrystal emission overlaps with the absorption spectra of the erbium [34]. This type of resonant energy transfer process appears to be responsible for only a small fraction of the excitation events.

2.4.5 SiGe Nanocrystal Luminescence Properties

The work in this thesis aims at understanding the energy transfer process between SiGe nanocrystals and Er. To support this research it is imperative that some background information be presented on SiGe nanocrystals and their luminescence properties. The SiGe system provides a new experimental parameter, since the band gap of this compound semiconductor may be altered by the choice of composition. The band gap may be tuned from 0.744eV (band gap of bulk Ge)[16] to 1.17eV (band gap of bulk silicon)[16]. Although this study is intended to add understanding to the relevant physics behind the energy transfer, the band gap control potentially enables the tuning of the band gap in resonance with Er transitions, possibly increasing the energy transfer rate.

SiGe nanocrystals are formed in a variety of ways. Similar to the fabrication of Si nanocrystals, SiGe nanocrystals can be formed by co-sputtering germanium along with silicon and silica, followed by an annealing step to induce nanocrystal nucleation and growth. This process usually requires annealing at temperatures above 800°C [35]. The formation of SiGe at temperatures as low as 550°C under UV illumination has been shown [36]. This method can be used to extend the thermal budget allotted for thermal processing of semiconductor chips. Either method

implemented for the fabrication of SiGe nanocrystals produces not only SiGe nanocrystals but also Si nanocrystals and Ge nanocrystals [35].

The photoluminescent properties of SiGe nanocrystal have been studied by several groups. It was found that SiGe nanocrystals display a broad photoluminescence peak in the between 1.2 eV and 1.5eV depending on Ge concentration. The luminescence has a typical FWHM of approximately 0.4eV. The nanocrystal related photoluminescence from these samples may be substantially red shifted by the inclusion of more excess germanium. It was also found that the inclusion of Ge in the Si nanocrystal system decreases the nanocrystal related photoluminescence and lifetime [37, 38]. In experiments conducted by Fuji on SiGe, it was found that the inclusion of Ge in the silicon nanocrystal system causes disorder in the nanocrystal lattice[39]. This disorder relaxes the k-conservation rule in the silicon nanocrystal leading to an increase in the optical transition oscillator strength. Electron spin resonant studies of SiGe nanocrystals created by the co-sputtering method reveal that the nanocrystals have many silicon and germanium related dangling bonds which may act as non-radiative centers for excitons created in the nanocrystal. It was observed that an increase of the Ge concentration resulted in an increase of the number of Ge related dangling bonds while the number of Si related dangling bonds remained the same [40].

CHAPTER THREE: METHODOLOGY

This chapter discusses the experimental setup and procedures employed in the current research.

3.1 Characterization and Modeling of the Sputter Deposition System

For thin film deposition, an AJA International sputter deposition system is used. This system has six independent sputter guns from which different materials may be deposited simultaneously onto a variety of substrates. Each gun may be driven with either a direct current (DC) or radio frequency (RF) signal depending on the target composition. An image of the system is shown in Figure 6.

Figure 6: The AJA International sputter system used in this research.

Sputter deposition is a process by which thin films can be fabricated based on bulk starting materials. During sputtering a plasma is concentrated near a piece of material which is to be deposited, called the target. The ions in the plasma remove atoms from the target which travel through the vacuum chamber and land on a substrate, resulting in the growth of a film with a composition similar to that of the target. A schematic diagram of a basic sputter system is shown below (Figure 7).

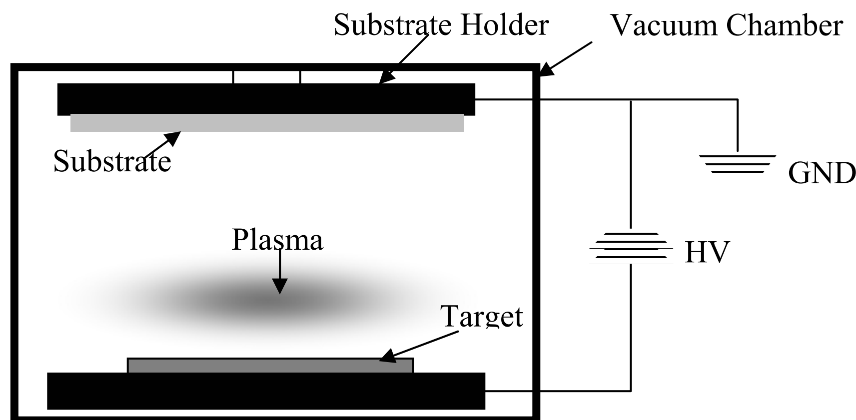

Figure 7: Basic sputtering system setup.

A basic sputtering system consists of a vacuum chamber that contains a high voltage source (HV) and a ground connection (GND). The vacuum chamber holds a substrate and a target material. In the multi target system used, each target is held in a cylindrical chimney with an automated shutter. The assembly of the shutter, chimney, target, and target holder is referred to as a sputtering gun.

The base pressure of the vacuum chamber before sputtering was approximately 10^{-8} mTorr. During sputtering, Argon is leaked into the chamber to a pressure of 4 mTorr. Argon is used as a sputtering gas because it is a noble gas with low chemical reactivity. To initiate sputtering, the

high voltage source is turned on and the target potential is lowered several hundred volts below the substrate potential. The large electric fields remove electrons from the argon atoms, generating Ar ions. The ionized gas is called a plasma. The positively charged argon ions are accelerated toward the target by the applied voltage, and upon impact detach atoms from the target, in a process called sputtering. The freed target atoms move toward the substrate and become the deposited film on the substrate.

The setup shown in Figure 7 works well for conducting targets, but is ineffective for insulating targets. This is because the insulating target becomes electrically charged upon the impact of each argon ion, effectively canceling out the applied field. To sputter from insulating targets the DC high voltage source is replaced by a RF source. This source alternates polarity at radio frequencies and thus avoids charging of the target.

Another challenge to sputtering from an insulating target is keeping the argon ions close to the target to avoid sputtering material from the gun assembly. To achieve this, magnets are placed behind the target as shown in Figure 8. This arrangement causes the charged argon ions to spiral around the magnetic field lines confining these ions close to the target surface. All of the guns used in the current setup have magnetrons behind them.

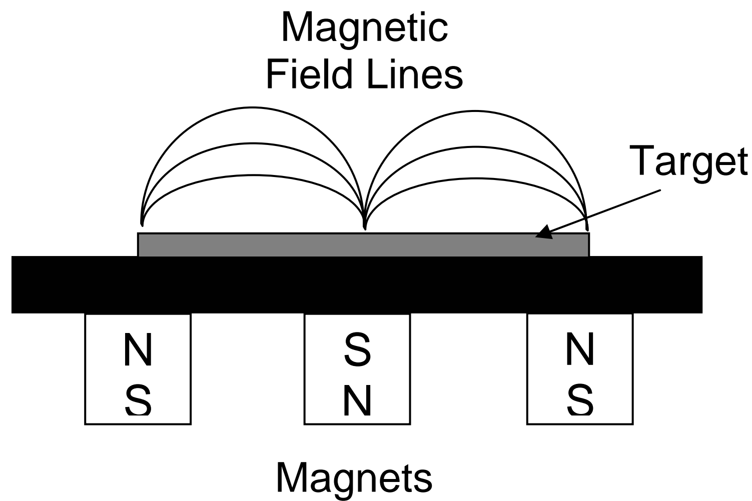

Figure 8: Diagram showing the arrangement of magnets behind the target in a magnetron gun

There are two ways to vary the composition of sputtered films on substrates. One method is to vary the composition of the target. In single target systems this can be accomplished by powder mixing followed by hot pressing, or by physically placing small pieces of a desired dopant onto a bulk sputter target. In the latter method, the amount of each material in the deposited thin film will be proportional to the ratio of the area taken up by that material to the total area of the target and the relative sputter rates at the provided sputter power. The use of multiple sputter guns, allows for greater flexibility in the film composition. In this case, the composition of the sample is controlled by changing the sputter power for each gun.

The achievement of well defined compositions requires calibration of the sputter system. It has been found that the sputter rate from each gun varies linearly with sputter power for a large range of powers. Below is a plot of measured sputter rates as a function of power on the respective targets used in these experiments, as obtained from the time dependent signal on a quartz crystal thickness monitor.

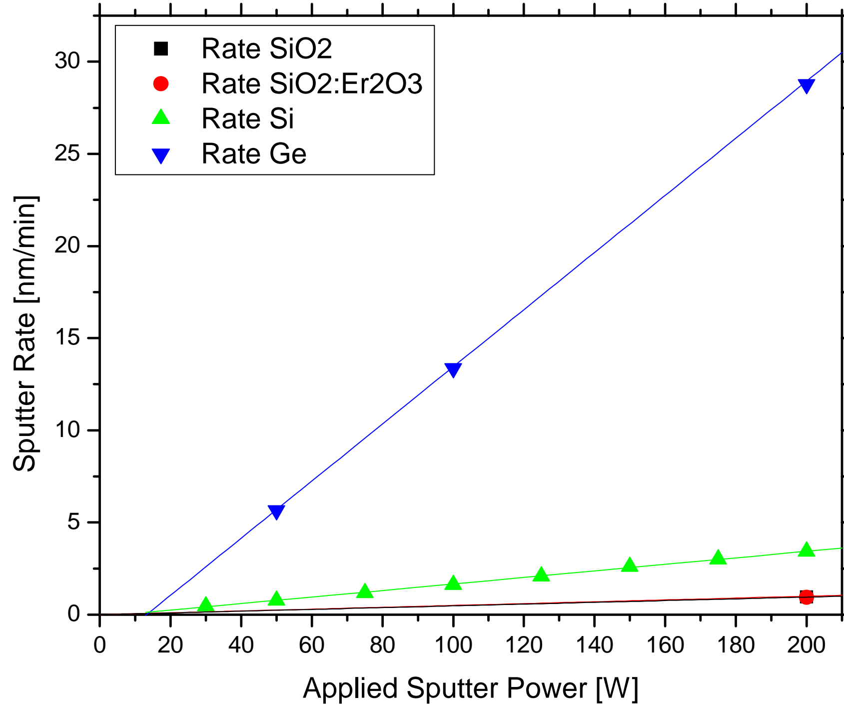

Figure 9: Relation between sputter rates and sputter powers for targets to be used in this experiment.

In order to obtain samples of specified composition an algorithm must be developed to calculate the required sputter powers for a given sample composition. The sputter process can be modeled by considering the composition of the targets and the sputter rate from each target. The number of atoms of a particular element in the deposited sample is given by Equation 32.

$$N_{Ele} = \sum_i R_i \rho_{Ele,i} t_i \quad (32)$$

Here R_i is the deposition rate from gun i in units of cm/min, $\rho_{Ele,i}$ is the atomic density of atoms of interest in target i in units of atoms/cm^3, and t is the number of minutes gun i was on. It is

assumed that all atom types sputter with the same probability, and have identical sticking coefficients on the sample. If more than one gun is used, the total concentration of each element involved can be written in matrix notation as shown in Equation 33.

$$\vec{N} = \hat{\rho}\vec{R}t \qquad 33$$

Where N contains the concentrations of each atom type on the sample, ρ is a matrix with matrix values ρ_{ij} where i corresponds to the target number and j corresponds to the relative concentration of each element in that target. The vector R represents the sputter rate from each target and t is the amount of time the system is sputtering. Equation 33 may be solved for the required sputter rates as a function of sample composition as shown in Equation 34.

$$\vec{R} = \frac{\vec{N}\hat{\rho}^{-1}}{t} \qquad 34$$

Often we are not concerned with the exact number of atoms of each element in the sample but the atomic percent makeup of the sample. Thus $\vec{N}$ may be normalized to 100 such that each component represents the atomic percent makeup of each element in the sample. If this is done the resulting array of relative rates $\vec{R}$ should be normalized to minimize the sputtering time without exceeding minimum or maximum allowed sputtering powers for each target.

In situations where the deposition rate of a given element is significantly higher or lower than that of other required target materials, the required powers might lie outside the achievable

system parameters. In this case a sputter mask was used on the target to increase the required sputter power above threshold. A mask containing an array of small apertures will block some of the material from the target and effectively reduce the sputter rate. In this way very low sputter rates may be achieved while running the sputter gun near its optimum power. For finely distributed apertures in a mask, the sputter rate is simply scaled by the fraction of open area in the mask. Equation 35 describes the sputter rates as a function of sputter power for a gun with a mask.

$$R = A_{O/T}\left(mP + b\right) \qquad 35$$

In this equation $A_{O/T}$ is the ratio of open area of the mask to total area of the gun opening, the sputter power of the gun (P) is in watts, and m and b are the experimentally determined calibration factors describing the relation between sputter power and sputter rate for a specified target.

Now that equations have been set up to describe the sputtering process an algorithm can be developed to determine the appropriate sputter parameters required to make a series of samples of a specified composition. A flow chart for such an algorithm is presented in Figure 10.

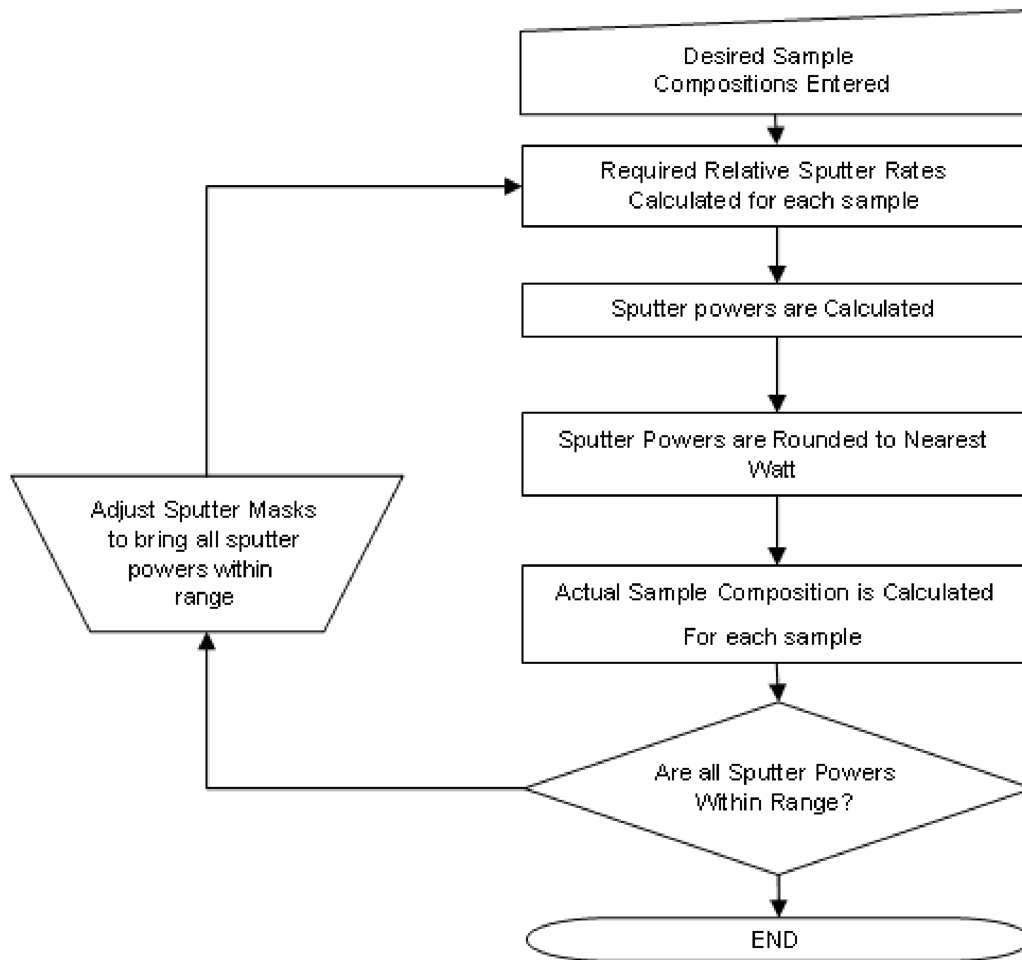

Figure 10: Flowchart showing the steps used to generate sputtering parameters from sample composition for a series of samples to be sputtered at the same time.

3.2 Design and Calibration of Thermal Treatment System

In order to activate the erbium in the sputter deposited films and to facilitate the nucleation of nanocrystals in group IV codoped samples, the deposited films must be annealed. To do this a controlled atmosphere thermal treatment system is used. The thermal treatment system used in this research consists of a Lindbergh tube furnace with a 3" diameter quartz tube. At one end of this tube is an adapter to the gas control system and at the other is the exhaust. The gas control system is used to regulate the flow of specified gasses through the system. It consists of a cylinder to store the gas, regulators to reduce the pressure of the gas to a useable level and a flow meter to measure and control the gas flow rate. The tube furnace is controlled by a Eurotherm 818 temperature controller.

It is important to know the temperature at the sample position. This temperature differs from the temperature as read from the furnace controller due to the intrinsic thermal gradient that exists in the furnace. For this reason a calibration was made of the temperature at the sample position as a function of the temperature reading at the temperature controller. After the furnace controller PID settings were optimized a k-type thermocouple was placed at the sample position and the furnace was set at various temperatures. At each set point the furnace was allowed to stabilize and a reading of the temperature at the sample position was recorded. The data from this calibration was fit with a line to find the actual sample temperature as a function of set point temperature. The raw data and calibration is presented below in Figure 11.

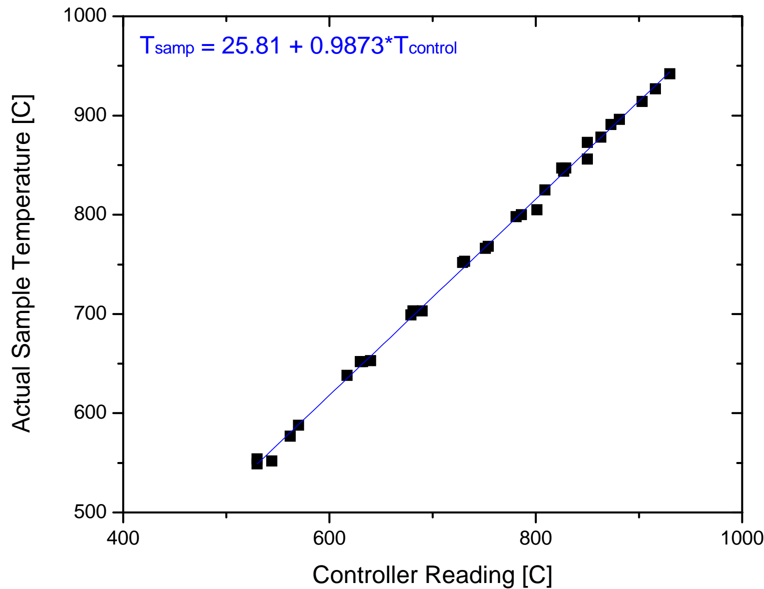

Figure 11: Calibration data and linear fit for the tube furnace

Annealing temperatures reported for samples in this research will be the temperature at the sample position. This temperature is found by reading the temperature from the furnace controller and converting this value to the temperature at the sample position by the calibration shown in Figure 11.

3.2 Sample Preparation

For the purpose of the current research ten films were deposited. Eight of these contain ~0.5 at.% Er, while two depositions did not include erbium for comparison purposes. Samples with different ratios of excess Si to excess Ge were deposited. A summary of the intended compositions of the samples is presented in Table 1.

Table 1: Composition of the samples used in this study.

Sample No.	01	02	03	04	06	10	99	100	102	106
Si [at.%]	30	32.5	35	37.5	31	33.2	27	32	40	31.8
O [at.%]	60	60	60	60	60	66.3	54	64	60	63.7
Ge [at.%]	10	7.5	5	2.5	9	0	0	0	0	0
Er [at.%]	0.5	0.5	0.5	0.5	0.5	0.5	0	0	0.5	0.5
Thickness [m]	1E-7	1E-7	1E-7	1E-7	1E-7	1E-7	1E-7	1E-7	1E-7	1E-7

Using the algorithm developed in section 3.1 that relates the requested sample composition to the sputtering parameters, the processing parameters for each sample were determined. The results of this analysis are presented in Table 2. Sputter masks were chosen to allow the deposition rate to be reduced so that the power on the SiO_2 target was maintained at 200W for samples 01 through 06. The required fraction of open area of the mask was found to be 0.33 for the silicon target and 0.015 for the germanium target. No masks were used in the deposition of samples 99, 100, 102 and 106.

Table 2: Deposition parameters for each sample composition of interest.

	Sample No.	01	02	03	04	06	99	100	102	106
Target Power [W]	Er_2O_3:SiO_2	68	85	82	81	85	0	0	126	111
	SiO_2	155	200	200	200	200	200	200	200	200
	Si	110	133	138	145	131	219	117	215	149
	Ge	152	143	98	55	173	0	0	0	0
	Deposition Time [min]	52	42	43	44	41	70	87	49	57

Samples were sputtered in a 4 mTorr argon atmosphere with an argon flow rate of 20 sccm. The system base pressure was 10^{-8} torr. In order to ensure that film thickness of 100nm, as recorded for each sample in Table 2.

In order to study the correlation between Er photoluminescence behavior and the presence of nanocrystals, samples from each wafer are annealed at different temperatures in the range 500°C – 1100°C for 30min in the controlled atmosphere tube furnace described in section 3.2. A typical annealing procedure is summarized as follows. The tube furnace is conditioned for at least 12 hours by flowing forming gas (a mixture of N_2 and H_2). The furnace is allowed to stabilize at the desired temperature for one hour and the gas flow rate is set to 65sccm. The samples are placed onto a quartz sample boat that is then loaded into the furnace. After 30min the samples are removed from the center of the furnace and brought near the end of the tube outside the heated region and are allowed to cool for 10min in flowing forming gas to minimize the risk of oxidation in air.

3.3 Compositional Analysis

In order to assess the composition of the as deposited films, Rutherford Back Scattering (RBS) spectrometry was used. In these measurements He^+ ions were accelerated to an energy of 2.2 MeV and directed toward the sample. These ions collide with sample atoms and recoil with a kinetic energy that depends on a) the mass of the sample atom they collided with and b) at what depth the collision occurred. Collisions with heavy elements will result in a high He^+ recoil energy while collisions with light atoms will result in reduced recoil energies. Secondly, collisions occurring at a finite depth into the sample will result in a lower recoil energy due to a combination of electronic and nuclear stopping. By measuring the recoil energies of a large collection of scattering events, a histogram of the kinetic energies can be generated, revealing information about the sample composition. To obtain values for the composition of our samples

this data is fit with a theoretical model provided in a program called the Rutherford Universal Manipulation Program (RUMP), which is a standard RBS analysis tool. Using RUMP, a simulated RBS spectrum can be generated based on an initial guess of the sample composition and thickness. By varying the various material concentrations and layer thicknesses, the data can be fitted manually in a few iterations. Using this method, the composition of the deposited films was determined. The fits of the RBS spectra for each of the deposited samples are shown in Appendix B. A summary of the RBS Results is presented in Chapter Four (Figure 13 and Figure 14).

3.4 Spectral Characterization of Er Doped Gain Media

The samples prepared in this thesis were investigated using photoluminescence measurements. Photoluminescence is the process by which light is absorbed at one wavelength and re-emitted at another. The spectrum of the emitted light is characteristic of electronic transitions in the luminescent material. Photoluminescence is studied by researchers to determine the optical properties of material systems.

The purpose of the photoluminescence setup is to stimulate and collect luminescence from a specific sample. In this type of setup a laser beam is focused onto the sample and partially absorbed by atoms in the sample. When these atoms de-excite they may emit light at different wavelengths and in all directions. A fraction of this light is then collected using a set of lenses and mirrors and analyzed using a monochromator and one or more light detectors.

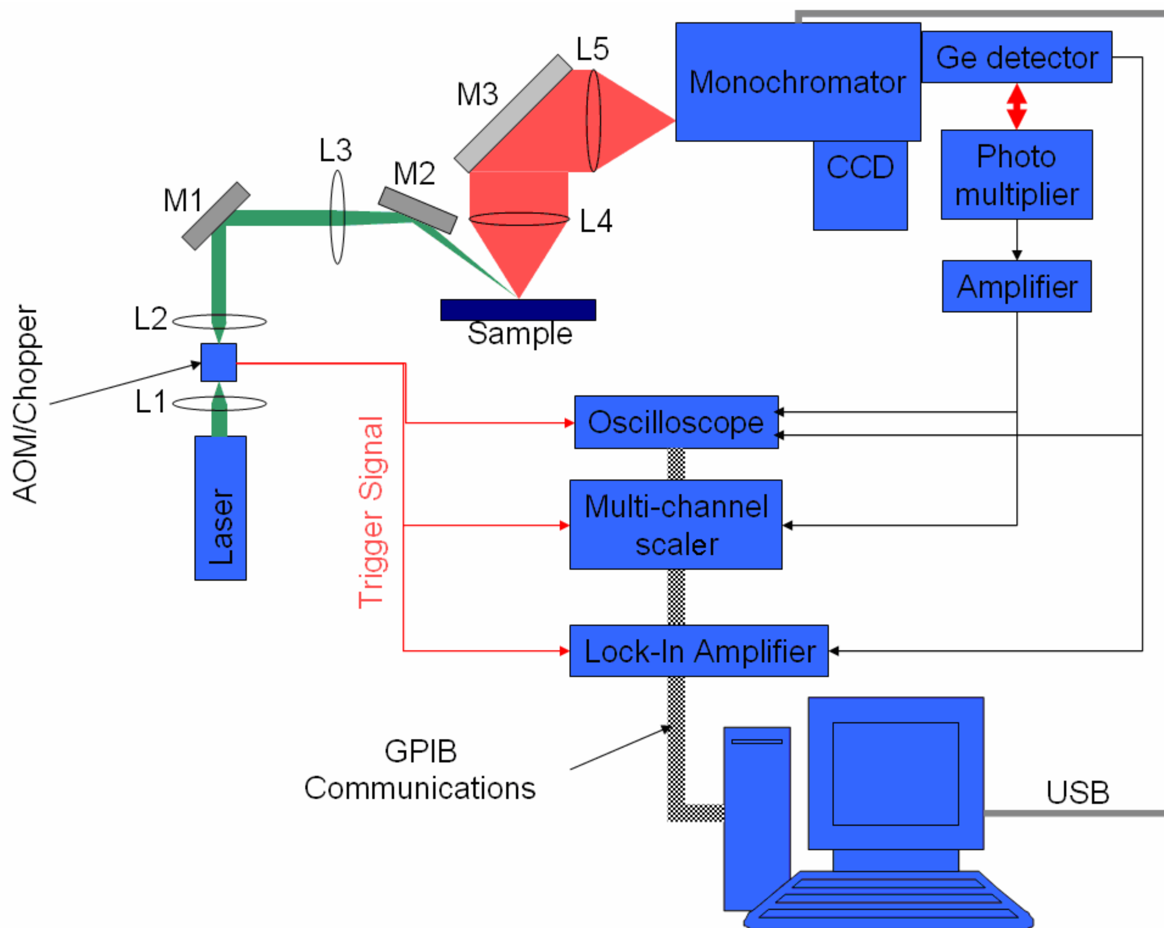

Figure 12: Optical system for the photoluminescence setup

A schematic diagram of the optical system used in the photoluminescence setup employed in the current research is shown in Figure 12. For lifetime measurements and phase sensitive detection the pump beam is modulated by a mechanical chopper or an AOM (Acousto-Optic Modulator). For lifetime measurements the pump beam is first focused onto the optical chopper or AOM by L1 and subsequently collimated by lens L2. This ensures the fastest cut-off time for use in lifetime measurements. The laser is directed toward the photoluminescence setup by mirror M1. Lens L3 then focuses the light onto the sample via mirror M2. The sample absorbs this light and emits at other wavelengths in all directions. Lens L4 collects the emitted photoluminescence

taking care not to collect the reflected laser. This light is then directed to the monochromator by M3. To match the f-number of the monochromator lens L5 is used. Optional filters (not shown) are placed before the entrance slits of the monochromator if necessary. The monochromator disperses the light and projects it onto either a CCD array for simultaneous collection of an entire visible spectrum, or to exit slits where a single element detector measures the relative intensities of the incident light as the grating scans the spectrum across the slits. A single element (non-pixilated) detector behind the exit slits is used for near infrared (NIR) spectral measurements and high speed signal detection. Time dependent measurements were performed with either a NIR sensitive Ge detector or NIR and VIS sensitive photomultiplier tubes (PMTs). Time dependent measurements using the Ge detector were recorded on a digitizing oscilloscope, while time dependent measurements using PMTs were recorded on a multichannel scaler. Spectral measurements in the NIR using the Ge detector were recorded via lock-in detection, where the chopper reference signal or the AOM driving signal were used as a trigger. Data collected by the oscilloscope, multi-channel scaler and the lock in amplifier were recorded by a computer running a LabVIEW code to control the experiments.

Photoluminescence measurements were performed using either a high power 975nm pump laser as an excitation source or using 568nm emission from a Kr laser as an excitation source. The 975nm wavelength was chosen as it coincides with the transition from the Er ground state to the $^4I_{11/2}$ state (2nd excited state). The 568nm wavelength was chosen as it does not overlap with any direct Er transitions. A long pass filter is placed in front of the entrance slits to block out any light that may be seen as second order light at the exit slits of the monochromator. For visible PL measurements a 150 l/mm grating was used with a 500nm blaze, while NIR measurements were

done with a 300 l/mm grating blazed at 1 μm. Typical entrance and exit slit widths were 1050μm corresponding to a spectral resolution of 10nm in the visible (λ = 1535nm) and 22 nm in the NIR (λ = 900nm). Visible photoluminescence spectra were collected using a 1024 pixel thermoelectrically cooled CCD array cooled to -80°C, located at the second output port of the monochromator. Photoluminescence spectra were corrected for the detector response as described in Appendix A. Temperature dependent photoluminescence measurements in the range 15K-300K are conducted in a closed-cycle helium cryostat.

CHAPTER FOUR: RESULTS AND DISCUSSION

4.1 Rutherford Back Scattering Results

The composition of the as deposited samples was verified using Rutherford Backscattering Spectrometry (RBS). The resulting RBS data and RUMP fits gathered from these experiments are presented in Appendix B. A summary of the results of these experiments is presented in Figure 13 and Figure 14.

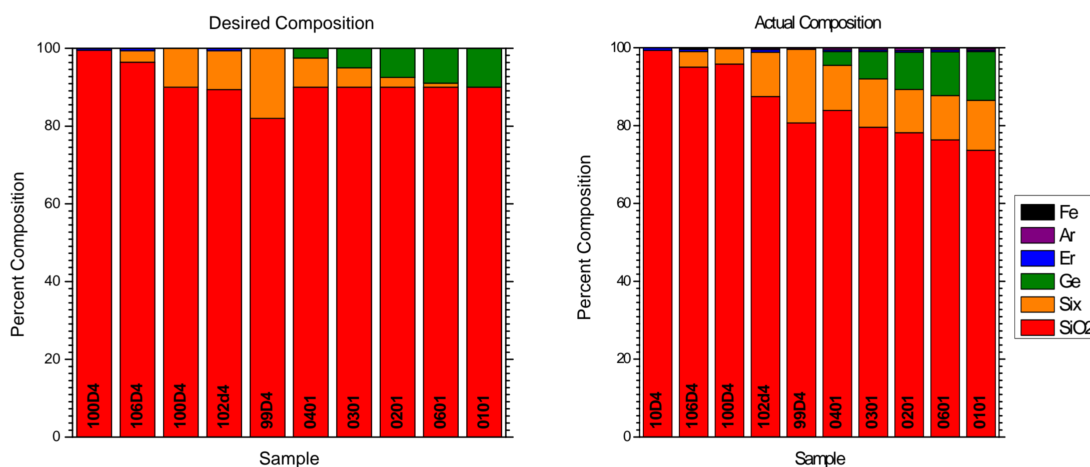

Figure 13: Desired and actual atomic percent composition of each sample deposited for annalysys in this report.The quantities of Ar, Er and Fe are less than 1 at.%.

Comparison of the two graphs in Figure 13 shows that the actual compositions of the deposited films differ from the desired composition for some samples in this series. The most notable are the four samples on the right have the greatest deviation from the desired composition. There are several possibilities for this discrepancy. From the five samples on the right it appears that the sputter algorithm was not changing the sputter power for the Si target enough to achieve the

desired composition. It is also observed that less oxygen is incorporated into films which are sputtered at a higher total rate. This indicates that oxygen is incorporated in to the films from the sputtering atmosphere. In order to achieve desired sample compositions in future depositions the incorporation of oxygen from the sputtering atmosphere must be taken into account. Although this was attempted in the present study, it appears that a sputter rate dependence of the oxygen incorporation that was not anticipated affected the results.

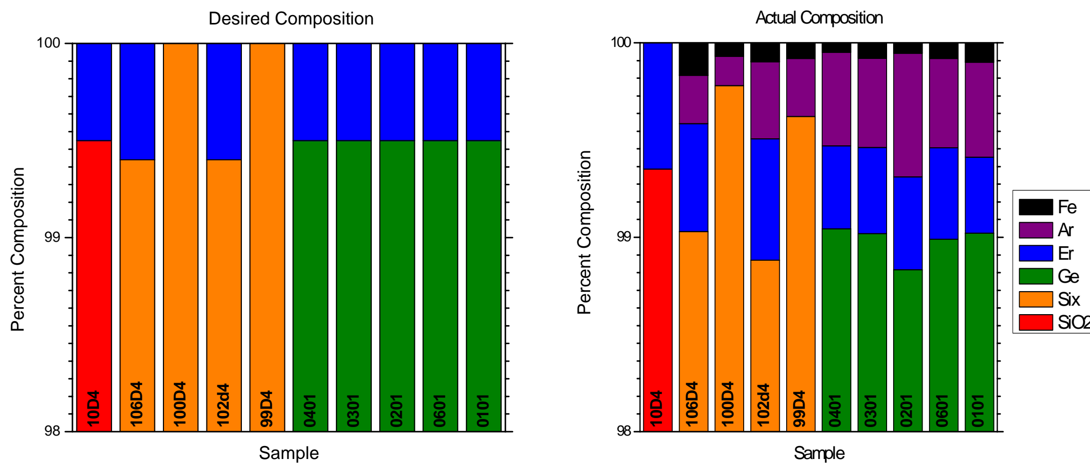

Figure 14: Detail of the desired and actual atomic percent of each sample deposited for analysis in this report. This graph shows trace quantities of iron and argon.

If we look in more detail at the compositions of the deposited sample (Figure 14) the existence of two contaminants can be seen. About one atomic percent of iron can be seen in all samples. The origin of this contamination is the dark shield being too far away from the target retaining ring in the sputter gun. This allowed plasma to form between the dark shield and the retaining ring and results in the sputtering of the stainless steel retaining ring. This is confirmed by a reduction in the iron signal when the dark shield is moved closer to the target retaining ring. Deposition of iron from this stainless steel retaining ring appears in the RBS measurements. While RUMP

analysis of the deposited films does not show the other components of stainless steel (Nickel and Chrome) they may be present in quantities which the RBS system can not detect.

The other contaminant found in these depositions was Argon. The Argon in the sample originates from the 4mtorr Argon atmosphere used to facilitate the sputtering process. Argon is an inert gas and is expected to have little effect on the performance of the films. Table 3 shows the actual composition of each of the samples as indicated by fitting of the RBS data.

Table 3: Composition of the samples used in this study.

Sample No.	01	02	03	04	06	10	99	100	102	106
Si [at.%]	37.41	37.15	38.97	39.54	36.80	32.80	45.83	35.92	40.54	35.65
O [at.%]	49.11	52.12	53.06	55.93	50.89	66.53	53.80	63.86	58.34	63.38
Ge [at.%]	12.50	09.55	06.99	3.57	11.30	00.00	00.00	00.00	00.00	00.00
Er [at.%]	00.39	00.48	00.46	00.43	00.47	00.65	00.00	00.00	00.62	00.55
Ar [at.%]	00.49	00.64	00.46	00.48	00.46	00.00	00.30	00.15	00.40	00.25
Fe [at.%]	00.10	00.05	00.08	00.05	00.08	00.00	00.08	00.07	00.10	00.17
Thickness [nm]	77.5	77.5	77.5	77.5	80.0	110	110	115	110	115

4.2 Photoluminescence Characterization

The visible photoluminescence spectra from samples annealed at different temperatures were acquired using the photoluminescence setup described in Section 3.5. Figure 15 shows the visible photoluminescence spectra for sample 04 with a composition of 11 at.% excess Si, 3.6 at.% excess Ge and 0.4 at.% Er in silica after different thermal treatments.

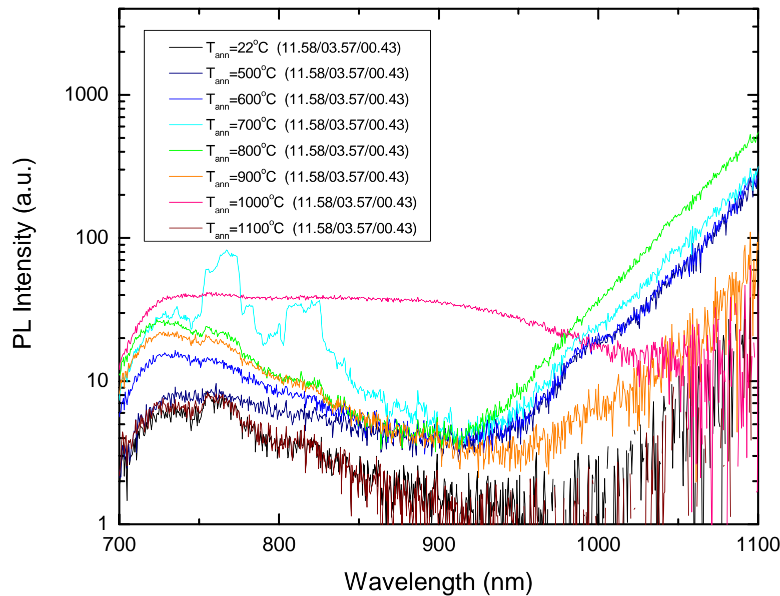

Figure 15: Visible photoluminescence spectra of sample emission when indirectly pumped with 568nm light. Nanocrystal emission is observed for the sample when annealed at 1000°C.

A broad luminescence band at short wavelengths is observed for all samples. This type of feature is commonly attributed to luminescence from defects in the oxide. This is confirmed by lifetime measurements at 750nm, showing a PL decay time faster than our system response time (0.3μs). Such fast decay is typical for emission from electronic defects in the amorphous SiO_2 matrix. The cutoff observed at the short wavelength side is due to the 700nm long pass filter in the collection path. The increasing emission band on the right side of Figure 15 is attributed to phonon assisted band edge luminescence from the Si substrate. For the sample annealed at 1000°C a broad emission band in the range 700-1000nm is observed. This type of emission band is commonly attributed to exciton recombination in nanocrystals, which are expected to form at temperatures in excess of 900°C.

The origin of the broad emission feature can be verified by performing temperature dependent photoluminescence measurements. Figure 16 shows multiple PL spectra of sample 04 at different sample temperatures ranging from 32K to 300K. The broad feature at 900nm attributed to nanocrystal luminescence is seen to initially increase in intensity as the sample temperature is increased from 32K to 100K, and to subsequently decrease as the temperature is raised from 100K to 300K. This trend is in agreement with the temperature dependent behavior observed in silicon nanocrystals as recorded in literature [28], and is caused by singlet triplet splitting of the excitons involved in the radiative transitions. Figure 16 thus provides indirect evidence that the sputter deposited samples annealed at 1000°C contain nanocrystals. Samples annealed at lower temperatures do not exhibit this type of emission, and are thought to contain only isolated excess Si and Ge atoms, or possibly few-atom clusters of group IV elements. These statements could be further verified using X-ray Photoelectron Spectroscopy (XPS).

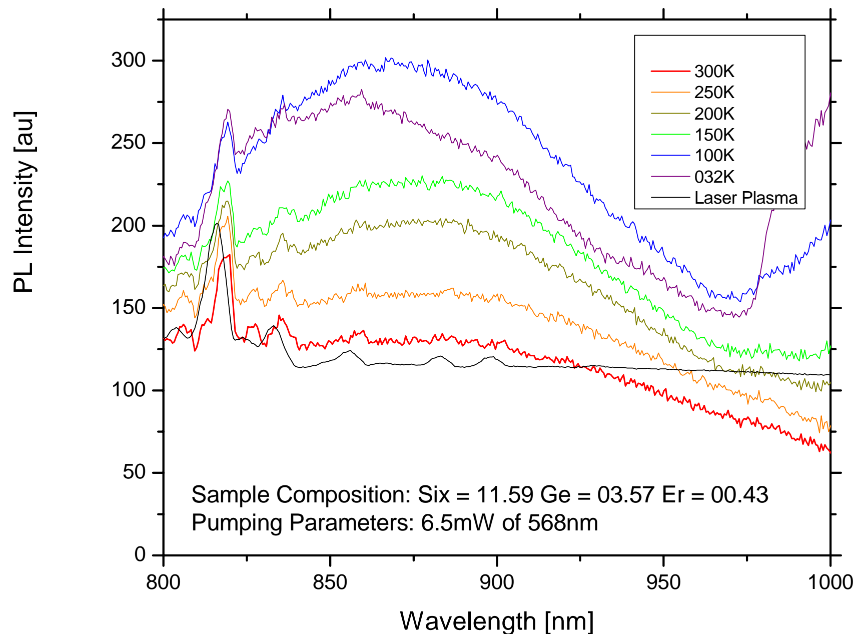

Figure 16: Temperature dependent visible photoluminescence spectra.

To study the effect of the film composition on the nanocrystal emission, samples with different composition were annealed at a temperature of 1000°C, and photoluminescence spectra were obtained under identical pump conditions. The results of these measurements are shown in Figure 17. Two things should be noted. First, the brightest PL intensity is obtained from a sample containing only excess silicon, while adding Ge is found to reduce the PL intensity. The relatively high intensity obtained from Si nanocrystals is tentatively attributed to the quality of the Si-SiO_2 interface. As mentioned in Section 2.4.5, the addition of Ge increases the number of dangling bonds at the nanocrystal surface, resulting in an increased non-radiative recombination of excitons in the nanocrystals. This reduces the quantum efficiency of the nanocrystal emission, resulting in a reduced PL intensity. Second, the redshift in the wavelength of maximum photoluminescence intensity is an indication that the nanocrystals containing a larger concentration of Ge or exhibit smaller quantum confinement. To distinguish these two effects, samples with a constant group IV concentration but a varying ratio of Si:Ge are required, which were not available in the present study.

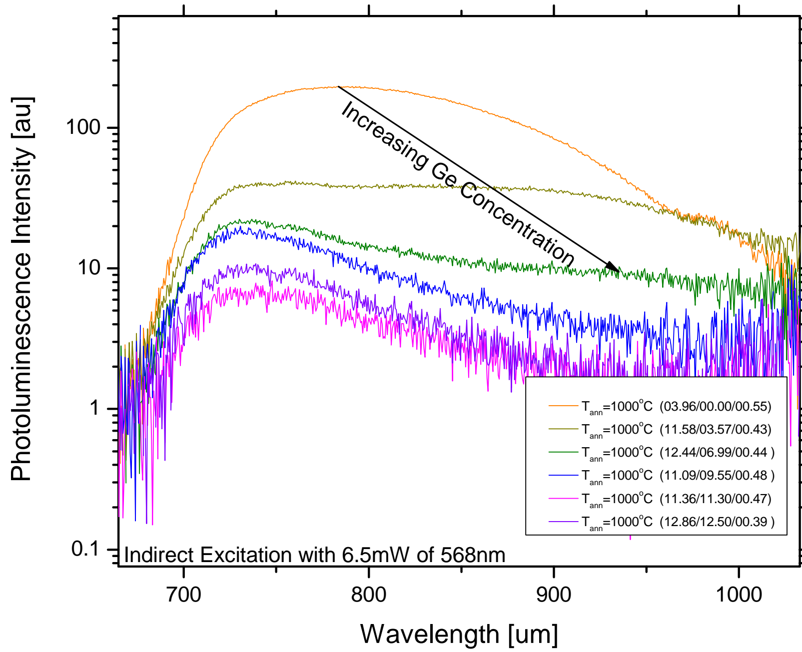

Figure 17: Temperature dependent visible spectra of sample emission.

4.3 Erbium Related Photoluminescence

Near-infrared photoluminescence spectra were collected while pumping either directly with a 975nm laser or indirectly using 568nm light. A typical photoluminescence spectrum of erbium in sample 04 is shown in Figure 18.

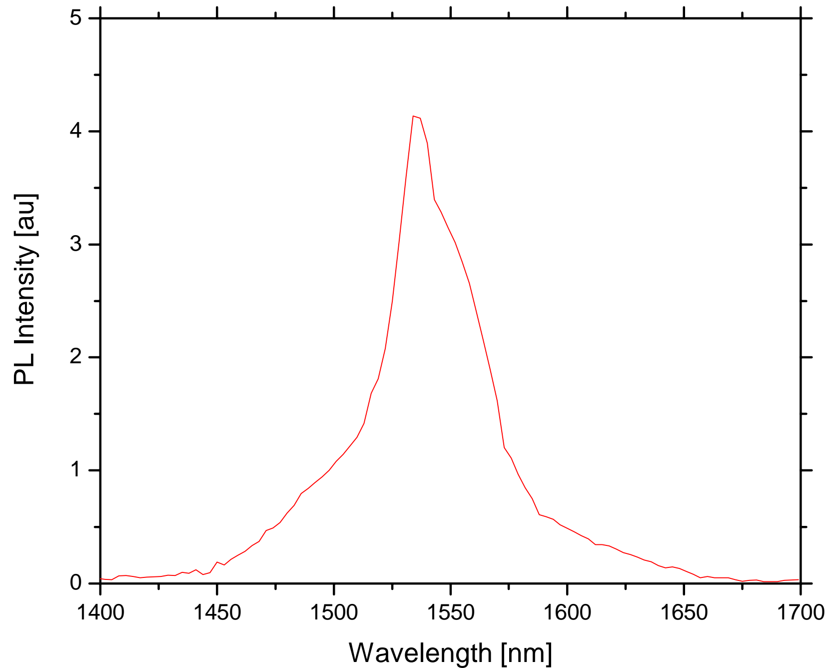

Figure 18: Typical Er spectrum of sample 04 pumped directly with 975nm laser light.

The peak Er related photoluminescence for each sample is plotted as a function of sample annealing temperature in Figure 19. An initial increase of the Er PL is observed as the samples are annealed at 500°C. This was the combined result of the oxidation of the Er in the film forming Er^{3+}, as well as the improvement of the SiO_2 host structure, resulting in a reduced density of electronic defects and an improved Er lifetime, as will be shown below. The former process is referred to as Er activation. As the thermal processing temperature increases from 500°C to 800°C the Er PL intensity continues to increase as the structure of the oxide improves[41]. As the processing temperature is increased from 800°C to 1100°C the Er related photoluminescence is seen to decrease, suggesting that Er^{3+} ions are lost or that the Er emission efficiency is reduced.

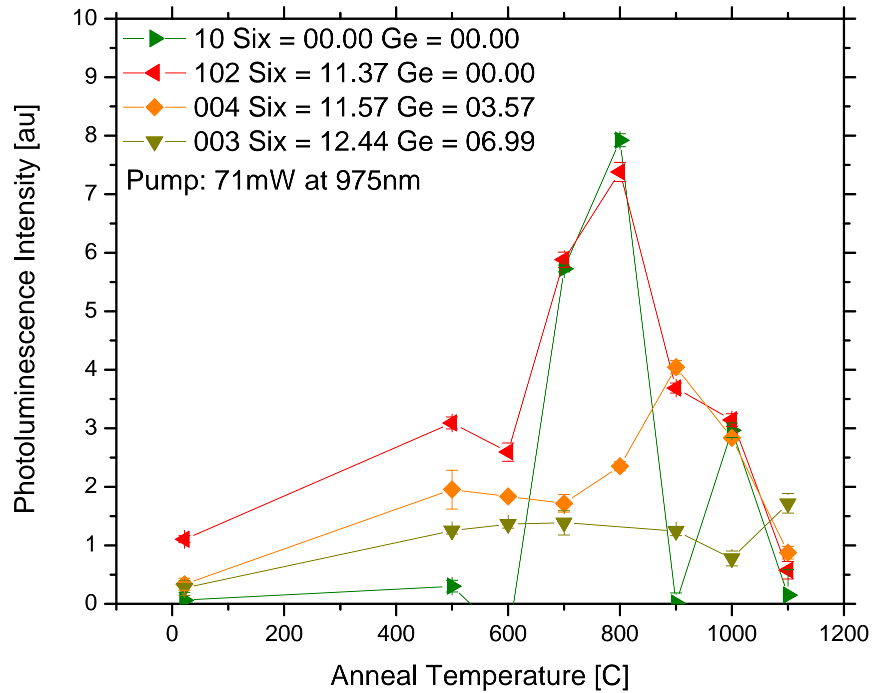

Figure 19: Peak Er related photoluminescence as a function of sample annealing temperature for samples of different concentrations.

To separate the effect of Er activation and changes in the PL emission efficiency, lifetime measurements of the Er related emission from for sample 04 ($Ge_{3.57}$:$Er_{0.43}$:$Si_{11.58}(SiO_2)_{27.97}$) were taken with a Hamamatsu NIR PMT. Fore these measurements a pump wavelength of 568nm was used, and the laser beam was modulated at 23 Hz. Figure 20 shows a lifetime trace of sample 04 annealed at 500°C along with the laser lifetime using the IR PMT and mechanical chopper.

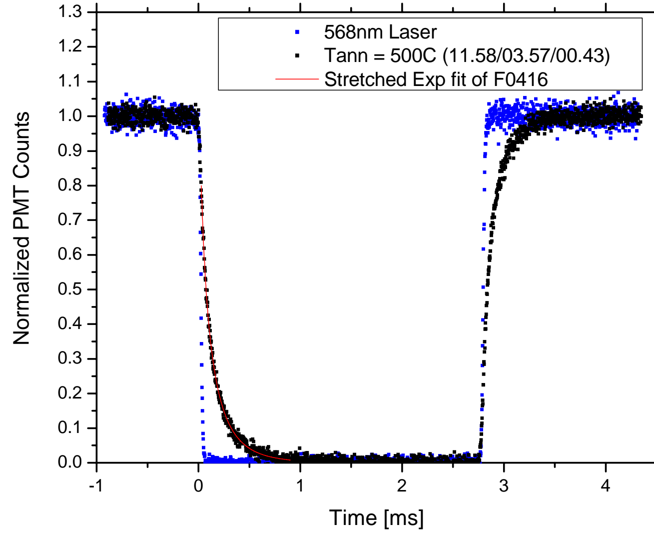

Figure 20: Typical Er related lifetime trace of sample 04 after a 500°C anneal as well as the 568nm laser lifetime. The sample lifetime is fit with a stretched exponential function.

The acquired lifetime traces were fit with a stretched exponential equation (Equation 36).

$$I = Ae^{-(t/\tau)^{\beta}} \qquad 36$$

The stretched exponential equation allows fitting of a non single exponential decay trace. Here τ represents the $1/e$ time of the photoluminescence, while the parameter β corresponds to the degree of non-exponentiality. A β of 1 corresponds to single exponential decay.

Figure 21 shows the measured PL intensity at 1.54μm and the fitted 1/e PL decay time as a function of annealing temperature. Both the PL intensity and lifetime increase up to an annealing temperature of 900°C. Above this temperature the PL lifetime continues to increase, while the PL intensity drops rapidly.

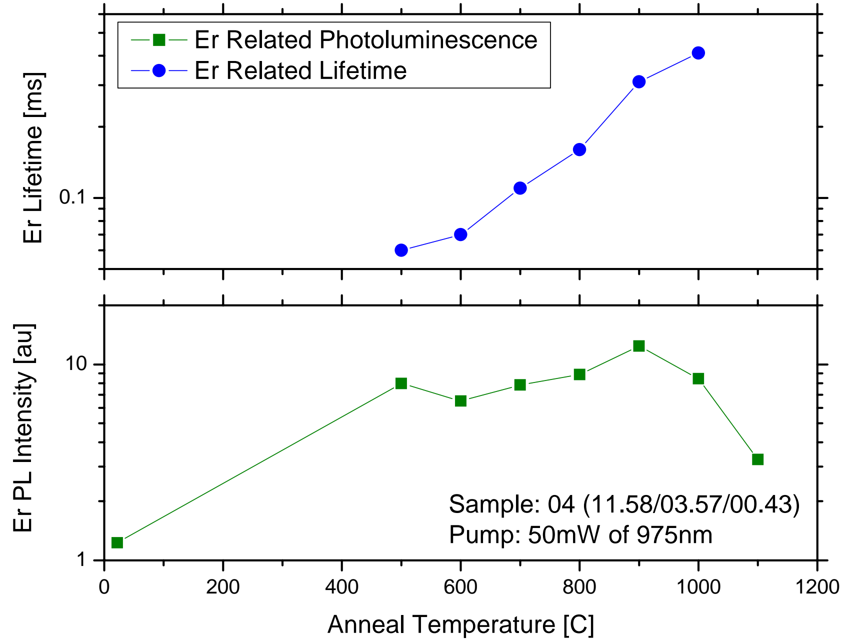

Figure 21: Comparison of trends in Er related photoluminescence and lifetime as a function of annealing temperature for sample 04.

The data presented in Figure 21 can be used to find trends in the Er active fraction as a function of thermal processing temperature. The photoluminescence intensity $I_{Er,d}$ of Er as a function of thermal treatment temperature when directly pumped with 975nm can be modeled using Equation 37.

$$I_{Er,d} \propto \sigma_{Erabs} \eta_{ErEmiss} f_{act} N_{Er} I_{975} \qquad 37$$

stating that at low pump power the Er PL intensity is proportional to the Er absorption cross-section at 975 nm (σ_{Erabs}), the emission efficiency $\eta_{ErEmiss}$, the Er active fraction f_{act}, the

concentration of erbium, and the pump irradiance I_{975}. Note that the subscript d is used to indicate direct excitation, while the subscript i will be used later to indicate indirect excitation. Equation 37 can be solved for the active fraction resulting in Equation 38.

$$f_{act} \propto \frac{I_{Er,d}}{\sigma_{Erabs}\eta_{ErEmiss}N_{Er}I_{975}} \qquad 38$$

The Er related absorption cross-section (σ_{Erabs}) is assumed constant. This assumption is reasonable since the Er related photoluminescence spectra taken for each sample were found to be similar, indicating a similar local environment in the SiO_2 matrix. Finally, the number of erbium ions is constant for each sample composition as a function of annealing temperature. These three observations simplify the result in Equation 38 to that in Equation 39.

$$f_{act} \propto \frac{I_{Er,d}}{\eta_{ErEmiss}} \qquad 39$$

The Er emission efficiency ($\eta_{ErEmiss}$) is given by the ratio of the radiative decay rate to the total decay rate (Equation 40).

$$\eta_{ErEmiss} = \frac{R_{rad}}{R_{rad} + R_{NonRad}} \qquad 40$$

The lifetime observed in PL decay measurements at 1535nm corresponds to the sum of the radiative and non radiative decay rates ($R_{rad} + R_{NonRad}$). Thus the excitation efficiency expressed in terms of lifetimes is given by Equation 41.

$$\eta_{ErEmiss} \propto \frac{\tau_{Er,d}}{\tau_{rad}} \qquad 41$$

As was mentioned in the introduction, the intra-4f transitions are parity forbidden, however interaction with the matrix material makes the transitions weakly allowed. The interaction with the matrix is reflected in the spectral shape of the Er emission line. Since the Er related photoluminescence spectra taken for each sample were found to be very similar, the local environment of the Er ions does not seem to be strongly annealing temperature dependent. For that reason we will simplify Equation 41 by assuming that the radiative lifetime of the Er is constant with annealing temperature (Equation 42).

$$\eta_{ErEmiss} = \tau_{Er,d} \qquad 42$$

Substituting this result into Equation 39 it is observed that the active fraction (f_{act}) as a function of annealing temperature is proportional to the Er related emission intensity as a function of annealing temperature and inversely proportional to the Er related lifetime as a function of annealing temperature (Equation 43).

$$f_{act} \propto \frac{I_{Er,d}}{\tau_{Er,d}} \qquad 43$$

The lifetime of the Er is assumed to be identical for direct and indirect pumping ($\tau_{Er,i} = \tau_{Er,d}$), and hence the above can be written as shown in Equation 44.

$$f_{act} \propto \frac{I_{Er,d}}{\tau_{Er,i}} \qquad 44$$

Based on the data presented in Figure 21, we can now find a relative measure of the Er active fraction as a function of annealing temperature. The result of this analysis is shown in Figure 22.

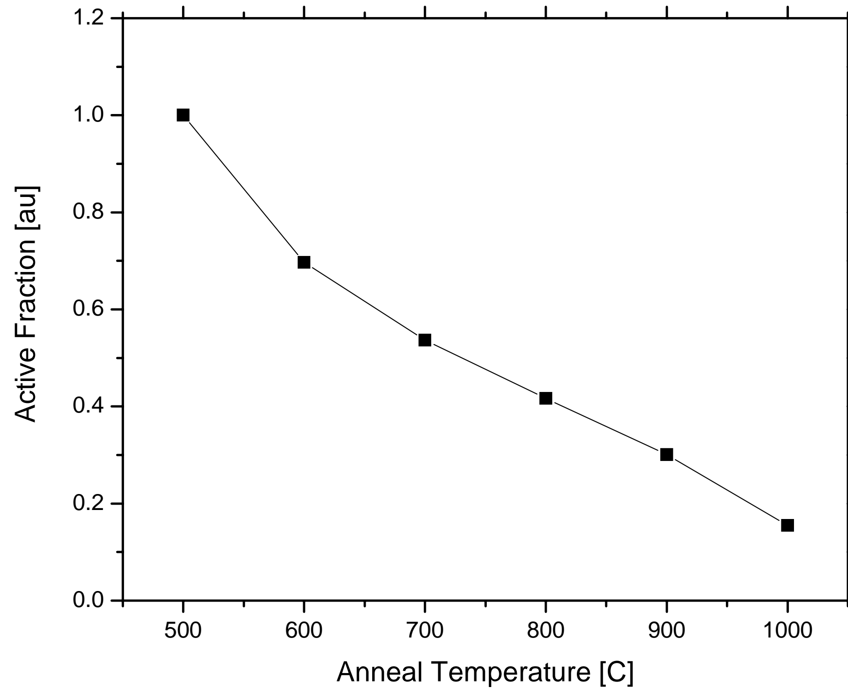

Figure 22: The active fraction as a function of annealing temperature for sample 04 ($Er_{0.43}Si_{11.58}Ge_{3.57}(SiO_2)_{28.14}$).

Figure 22 shows a reduction of the number of active Er^{3+} ions in the oxide matrix. This is commonly seen in the annealing of Er doped glasses containing high concentrations of Er (C_{Er} > ~0.1 at.%). At high annealing temperatures significant Er diffusion can occur, resulting in Er segregation, into high Er concentration regions, an effect known as 'clustering'. Clustering is commonly expected at higher annealing temperatures but could occur at lower temperatures because of the non stoichiometric mix of SiO_2. Clustering results in the formation of Er rich areas and a loss in the concentration of optically active Er^{3+}[42].

As was mentioned in Section 2.4 the presence of group IV nanocrystals is expected to result in indirect excitation of Er. In order to study the contribution of nanocrystal mediated excitation in these samples, the Er related photoluminescence was measured using an excitation wavelength of 568nm. This wavelength does not overlap with a direct Er absorption line, and consequently any observed Er emission can be attributed to indirect excitation. The results of these measurements are summarized in Figure 23. It should be noted that these results have been normalized to the incident pump photon flux in photons/s, allowing a direct comparison between the intensities in Figure 19 and Figure 23. A first thing to notice is the increased Er related photoluminescence intensity for samples containing excess group IV material. No Er related photoluminescence was observed from samples not containing excess group IV material (▶), confirming that excess group IV material is required for Er sensitization. In samples containing excess silicon only, indirect pumping increases the Er related photoluminescence by an order of magnitude compared to direct pumping of the samples (1000°C anneal).

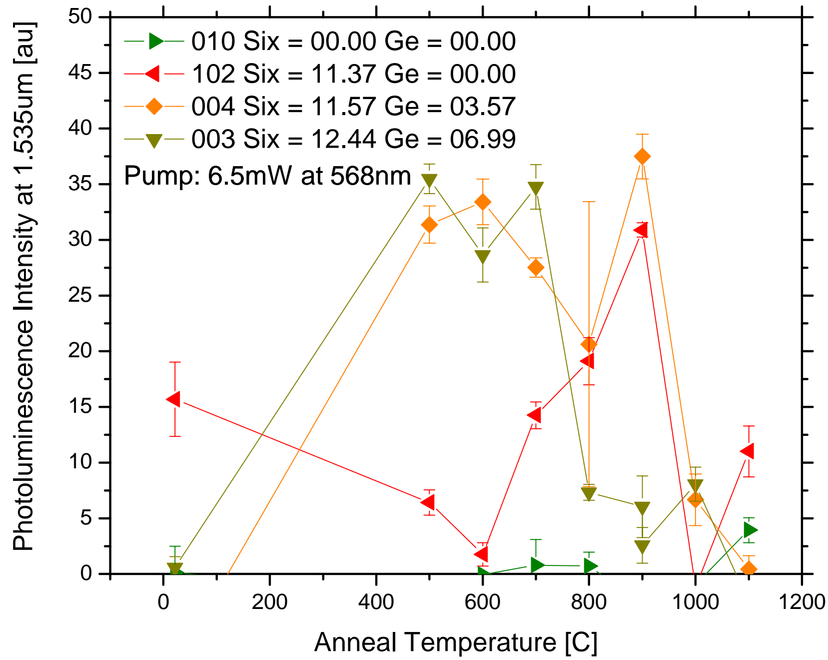

Figure 23: Photoluminescence intensity as a function of thermal processing temperature for samples of diffrent compositions.

The fact that the maximum enhancement in the sample containing only excess Si (Sample 102) and the appearance of nanocrystal related emission feature occur at the sample annealing temperature of 1000°C seems to suggest that the enhancement requires the formation of silicon nanocrystals. Surprisingly, significant indirect excitation is observed at lower annealing temperatures as well. Nanocrystals are not known to form at these low temperatures and the absence of any nanocrystal related luminescence from these samples suggests an alternate sensitization mechanism is responsible for the observed indirect excitation. In samples containing 11.58 at.% excess Si and 03.57 at.% excess Ge a similar trend in photoluminescence intensity is observed, however the peak value is reached at much lower temperatures (500°C). In the Ge doped samples, the known appearance of a nanocrystal related emission band after

annealing at 1000°C does not appear to affect the Er luminescence intensity, but instead is accompanied by a strong reduction in the Er PL intensity, partly attributed to erbium clustering. These results indicate that both in Si and SiGe doped SiO_2, the presence of nanocrystals is not essential in the sensitization of Er. To further corroborate this hypothesis excitation spectra were taken of samples of the same composition ($Er_{0.43}Si_{11.58}Ge_{3.57}(SiO_2)_{28.14}$) after being annealed at 500°C, 800°C, and 1000°C to compare the behavior of the Er related emission (Figure 24). The samples annealed at 500°C and 800°C show no sign of nanocrystal related emission., while the sample annealed at 1000°C shows nanocrystal emission in the region of 750nm to 1000nm. It is observed that the samples that do not show the presence of nanocrystals exhibit the same excitation spectra as samples which do show nanocrystal emission. This observation further suggests that the presence of nanocrystals is not necessary for indirect excitation of erbium.

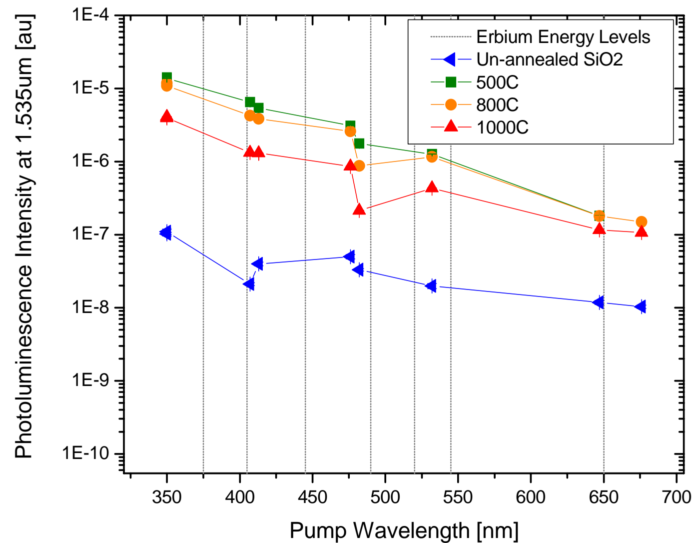

Figure 24: Excitation Spectra for Sample 04 ($Er_{0.43}Si_{11.58}Ge_{3.57}(SiO_2)_{28.14}$) for samples annealed at different temperatures as compared to the absorption spectra of erbium in a silica glass.

This is tentatively attributed to the existence of few-atom clusters or excess Si and Ge related electronic defect levels in the SiO_2 matrix that act as *e-h* recombination sites. Further studies are required to determine the exact mechanism responsible for this indirect excitation.

The data presented in Figure 19, Figure 21, and Figure 23 can now be used to find trends in the Er effective erbium cross section as a function of thermal processing temperature. The effective erbium cross section here is defined as the apparent absorption cross section of the erbium under indirect excitation. It includes the effects of the sensitizer cross section, the number of sensitizers per unit volume N_{sens}, and the energy transfer efficiency. In the case of indirect pumping using 568nm light the Er PL intensity is given by Equation 45.

$$I_{Er,i} \propto \sigma_{sens} N_{sens} \eta_{trans} \eta_{ErEmiss} f_{act} N_{Er} I_{568} \qquad 45$$

Here σ_{sens} represents the absorption cross-section of the sensitizing element at a wavelength of 568nm, and η_{trans} represents the energy transfer quantum efficiency. Substituting Equation 44 for f_{act} into Equation 45 results in Equation 46.

$$I_{Er,i} \propto \sigma_{sens} N_{sens} \eta_{trans} \eta_{ErEmiss} N_{Er} \frac{I_{Er,d}}{\tau_{Er,i}} \qquad 46$$

Substituting our previous result $\eta_{ErEmiss} \propto \tau_{Er,i}$ in Equation 46 and assuming constant N_{Er}, Equation 47 is obtained.

$$I_{Er,i} \propto \sigma_{sens} N_{sens} \eta_{trans} I_{Er,d} \qquad 47$$

This equation can use to find the effective indirect excitation cross-section σ_{eff}, the product of the number of sensitizers per unit volume, the Er related excitation efficiency and the sensitizer absorption cross-section as shown in Equation 48.

$$\sigma_{eff} = \sigma_{sens} N_{sens} \eta_{trans} \propto \frac{I_{Er,i}}{I_{Er,d}} \qquad 48$$

A plot of this quantity is shown in Figure 25 for sample 04 (11.58/03.57/00.43). This plot confirms that the formation of nanocrystals, which occurs at an annealing temperature of 1000°C, does not produce a strong effect on the effective absorption cross-section enhancement.

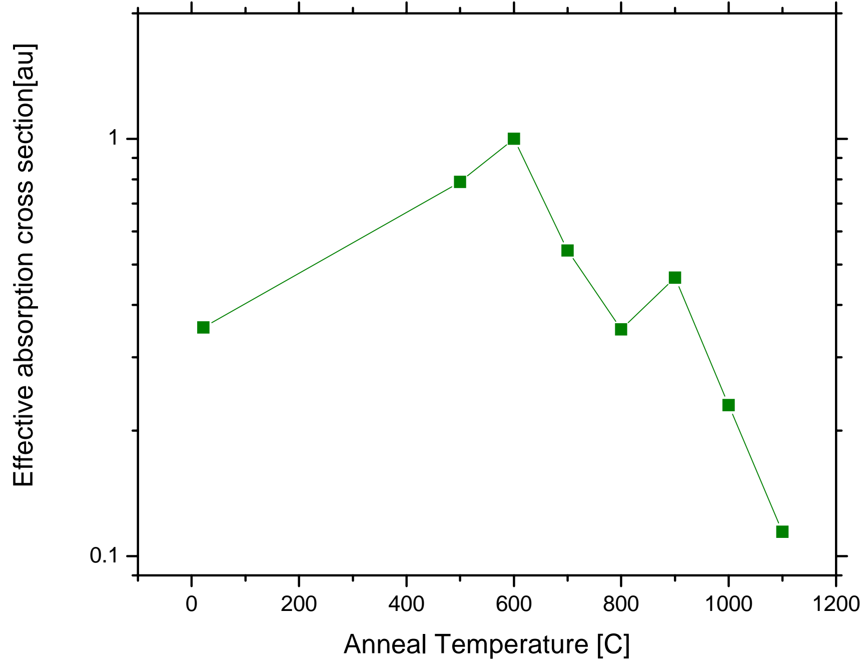

Figure 25: The product of the cross-section and excitation efficiency as a function of annealing temperature for sample 04.

To verify the analysis followed above, the effective Er excitation cross-section is calculated independently using rise and decay time measurements. For a quasi two level system and assuming a fixed number of Er ions per sensitizer, the excitation cross-section is found to be proportional to the difference between the rise and decay rate (Equation 49).

$$\sigma_{sens} \propto \frac{1}{\tau_{Up,i}} - \frac{1}{\tau_{Dn,i}} \qquad 49$$

Figure 26 superimposes the results from Figure 25 and the results obtained from Equation 49. The agreement between these curves suggests that there is little change in the product $N_{sens} \times \eta_{trans}$ as a function of annealing temperature.

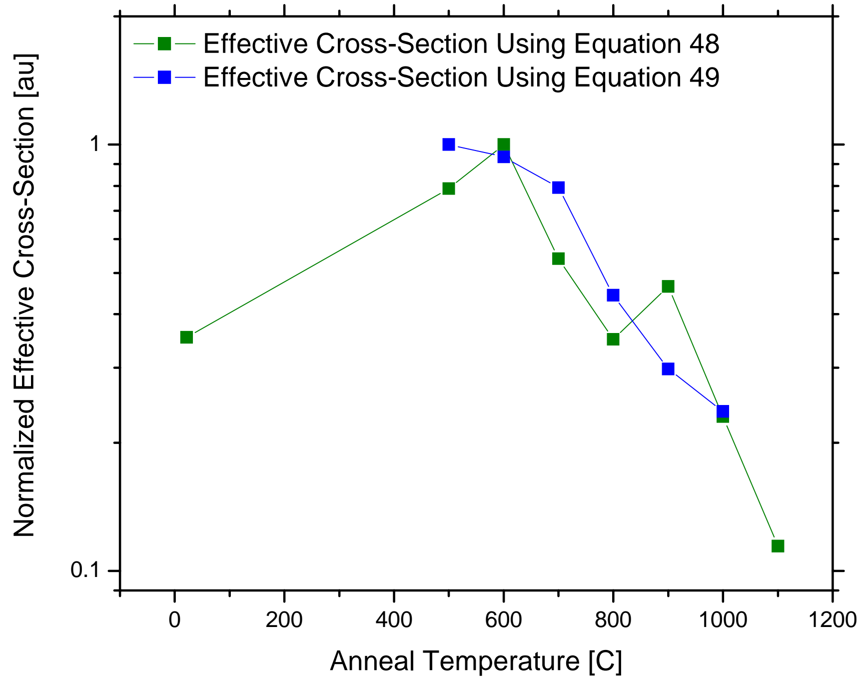

Figure 26: Comparison of the effective cross-section calculated using two different methods.

The analysis above shows that all Er doped group IV codoped samples in which Er PL could be detected exhibit indirect Er excitation at low annealing temperatures. To look more closely at the effect of Ge doping, Figure 27 shows the Er related photoluminescence intensity as a function of Ge concentration for samples annealed at different temperatures. At low annealing temperatures, increasing the Ge concentration from 0 at.% Ge to 3.6 at.% is seen to enhance the Er PL intensity, however the addition of more Ge reduces the PL intensity. At higher annealing temperatures, the addition of more Ge appears to result in a reduced PL intensity at lower Ge

concentrations. Since adding Ge and annealing at higher temperatures both are expected to result in the formation of larger nanoclusters, the data in Figure 27 seem to indicate that the formation of large clusters is detrimental to the indirect Er excitation.

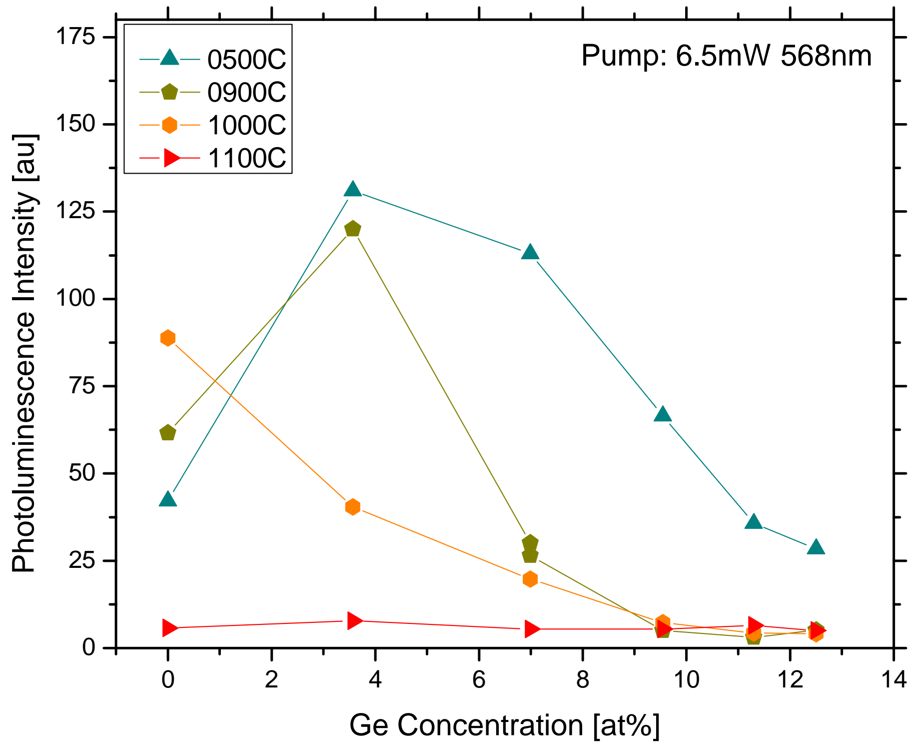

Figure 27: Er related photoluminescence as a function of Ge content for samples annealed at various temperatures.

CHAPTER FIVE: SUMMARY

In this thesis the effect of Ge doping on silicon rich silica thin films doped with Er was studied. Thin films of various compositions were deposited by means of sputter deposition. The films were annealed at various temperatures to activate the Er and to initiate the nucleation and growth of semiconductor nanocrystals. The presence of nanocrystals in films containing 12% excess Si and Ge concentrations in the range 0-11 at.% when annealed at 1000°C for 30 min in forming gas was confirmed via room temperature photoluminescence (PL) measurements. Temperature dependent PL measurements on a sample containing 3.6 at.% Ge annealed at 1000°C revealed behavior characteristic of exciton recombination, further supporting the presence of semiconductor nanocrystals is these samples. A red shift in the peak emission wavelength of nanocrystal doped samples containing higher concentrations of Ge suggests that Ge may be incorporated into the nanocrystals, resulting in a reduced bandgap. Part of the red shift may be attributed to an increased nanocrystal diameter. Further studies are required to distinguish the effects of SiGe alloying and quantum confinement.

Measurements of the Er photoluminescence intensity and lifetime under direct excitation of the Er ions as a function of annealing temperature indicate that Er clustering is limiting the photoluminescence intensity from samples annealed at higher temperatures. Comparison of the Er PL intensity under two different excitation conditions were used to determine the effective Er excitation cross-section enhancement as a function of annealing temperature. For samples that show Er PL it is found that the Er excitation cross-section is enhanced by up to an order of magnitude by the presence of group IV excess material. These observations are confirmed by an

independent determination of the excitation cross-section using time dependent photoluminescence measurements. Significant cross-section enhancements are observed at temperatures well below those required for the formation of semiconductor nanocrystals. This indicates that the formation of nanocrystals is not a requirement for sensitization of Er, suggesting that another type of sensitizer contributes to the Er photoluminescence enhancement. Possible candidates are electronic levels deep in the oxide band gap due to the presence of Si and Ge dopants, or few-atom semiconductor clusters embedded in the oxide matrix. The achievement of Er sensitization at process temperatures as low as 500°C could substantially improve the usability of these compounds in Si electronics, since these annealing temperatures do not significantly affect the electronic properties of Si. Further studies should aim at simultaneously optimizing the effective excitation cross section as well as the Er PL efficiency.

At low annealing temperatures ($T_{anneal} < 1000°C$) the addition of 3.6 at.% Ge to samples containing 12 at.% excess Si is found to increase the Er PL intensity when excited at 568nm. The Ge could be incorporated into the silica matrix in three different forms, as SiGe nanocrystals, as a Ge dopant level, or as Ge nanocrystals. While it is observed that small amounts of Ge can increase the Er sensitization, the actual role of the Ge in Er sensitization requires further investigation.

APPENDIX A: SPECTRAL CALIBRATION OF PHOTOLUMINESCENCE SETUP

To calibrate this system one must obtain a calibration source. That is a source for which the spectral irradiance is known. Often a quartz tungsten halogen lamp is used for calibration along with a stable power supply. The tungsten halogen source gives broad spectra as shown in Figure 28 and the quartz has no sharp absorption lines in a large range of use. The calibrations made in this study use an Oriel # 63350 quartz tungsten halogen lamp along with a Oriel Radiometric Power Supply. This lamp has a smooth black body spectrum shown in Figure 28 and is described by Equation 50

$$\text{Irradiance}\,(\text{mW/m2 nm}) = \lambda^{-5} e^{\left(A + \frac{B}{\lambda}\right)} \left(C + \frac{D}{\lambda} + \frac{E}{\lambda^2} + \frac{F}{\lambda^3} + \frac{G}{\lambda^4} + \frac{H}{\lambda^5} \right) \qquad 50$$

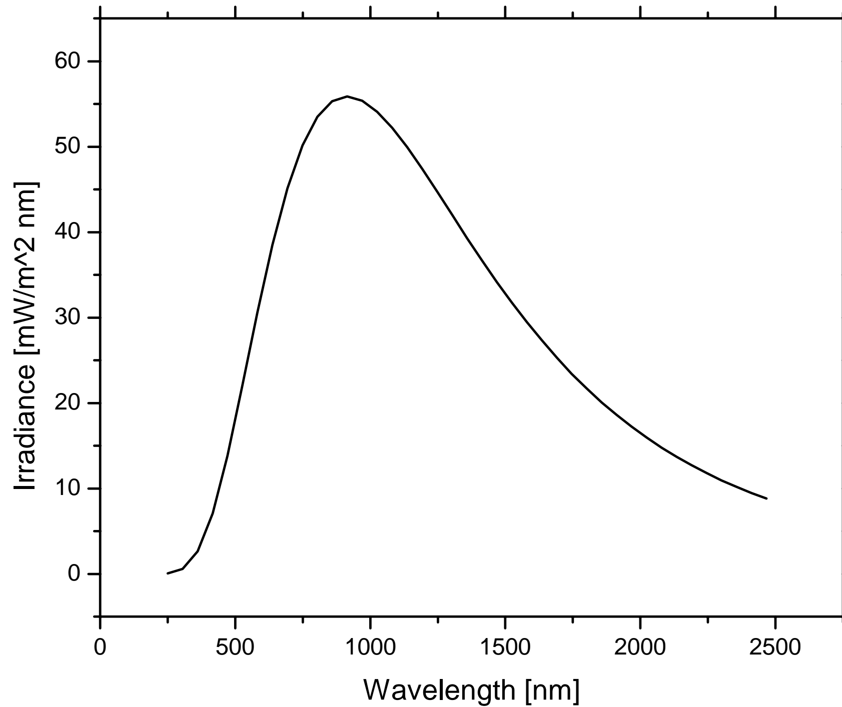

Figure 28: Black body spectra of the calibration lamp.

The coefficients (A through H) for this study are provided by the lamp manufacturer. Table 4 summarizes the constants used for the presented calibration.

Table 4: Coefficients for model of calibration lamp intensity.

A	4.31E+01	E	-2.13E+05
B	-4564.880499	F	7.35E+07
C	9.08E-01	G	-9.26E+09
D	2.45E+02	H	0.00E+00

For the calibration of our detectors the lamp was placed 21 inches from the entrance slits of the monochromator, a pinhole aperture (1mm diameter) was placed 9.5 inches away from the lamp. The optional long pass filters were placed just in front of the monochromator entrance slits to remove second order light at longer wavelengths. A top view image of the calibration setup is shown in Figure 29 and an oblique view in Figure 30.

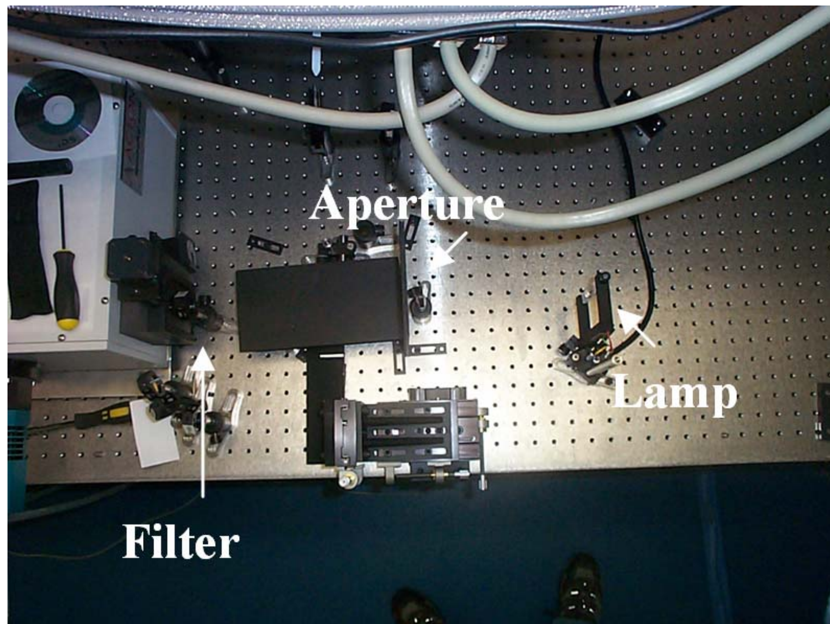

Figure 29: Top view of the experimental setup

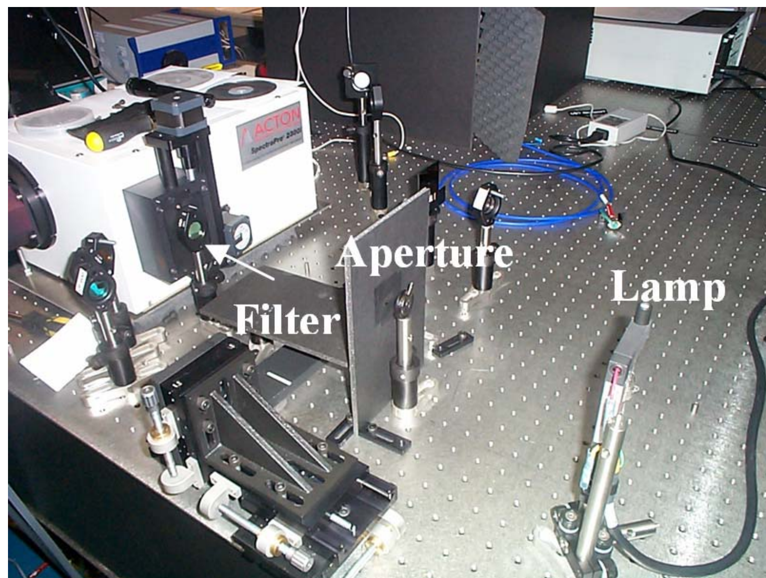

Figure 30: Oblique view of the experimental setup

A blazed grating sends 100% of the design wavelength into the first order. The diffraction efficiency for wavelengths other than the design wavelengths is slightly worse. Thus light at wavelengths other than the design wavelength may appear in the spectra at twice the wavelength

and is known as second order light. This light can be removed by using a long pass filter. This will allow the user to obtain accurate spectra where second order light may appear.

Calibration of the Germanium Detector

Figure 31: The germanium detector.

Calibration of a single element detector is somewhat simpler than that of a CCD array. This has much to do with the fact that there is only one detecting element as apposed to many. Figure 32 shows a schematic diagram of the optical path for a Czerny-Turner grating monochromator and single element detector.

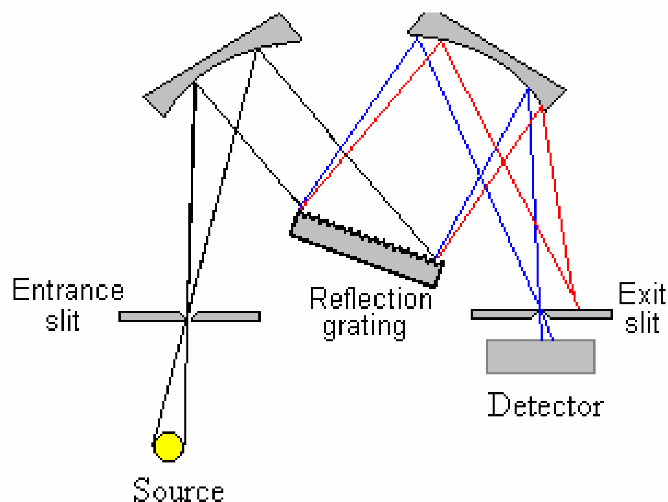

Figure 32: Czerny-Turner grating monochromator and single element detector.

In this setup the reflection grating is rotated to cause the different wavelengths to hit the exit slit opening and a measurement of the intensity of each wavelength is recorded at the detector. Often

a blazed grating is used in this setup. Blazed gratings are manufactured to have 100% diffraction efficiency at a design wavelength. For example a 500nm blazed grating will predominantly diffract 500nm light into the first order. There are three gratings that may be used in the current setup. The first is a 300 lines/mm 500nm blazed grating for detailed spectroscopy of the visible region. The second is a 300 lines/mm 1000nm blazed grating for detailed spectroscopy of the inferred region and the third is a 150 lines/mm 500nm blazed grating for overview spectra of the visible region.

For the calibration of the germanium detector a 900nm and 1200nm long pass filter was used to ensure that second order light is not included in the calibration. Spectra of the calibration source were taken in the range of 200 – 1800nm with each of the long pass filters (900nm LPF and 1200nm LPF) for each of the three gratings (300 lines/mm 500nm blazed, 300 lines/mm 1000nm blazed, and 150 lines/mm 500nm blazed). In addition to this, a spectrum with no long pass filters and a dark spectrum were taken, resulting in a total of ten spectra. Each spectrum was taken at a resolution of 6nm +- 1nm. In regions with sharp spectral features another spectrum was taken at higher resolution to measure the spectral profile more accurately. This technique can be seen in Figure 33.

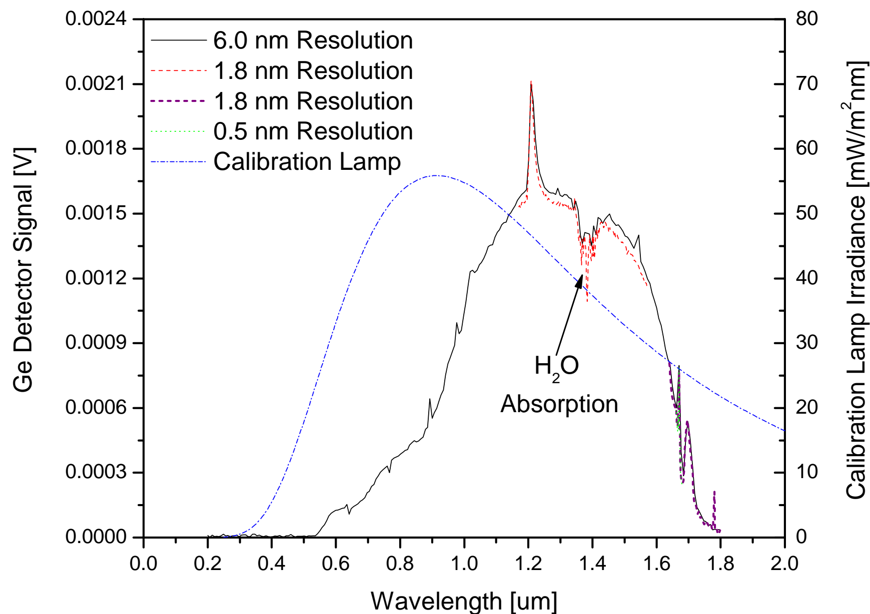

Figure 33: Spectra of calibration lamp using the germanium detector, no long pass filter and a 300 line/mm 500nm blazed grating. The actual calibration spectrum is also plotted. This graph demonstrates the use of different resolutions to pick out finer features.

One can see from the graph that a peak around 1.2µm is real since two scans with different resolution reveal the same peak. This peak is due to the response of the grating detector system. The dip around 1.4µm is also real and attributed to absorption by vibration modes of water in the atmosphere. The typical building relative humidity is 43% and the total beam path is 147cm. Further, the feature at 1.67 µm is real and is a response of the grating detector system. The germanium detector is known to send out erroneous signal spikes on occasion. According to the manufacturer this may be due to muons hitting the active area of the detector or the detector electronics. These large spikes have been removed before data analysis.

Following are plots of the intensity versus wavelength for spectra taken with 1) no long pass filter, 2) a 900nm long pass filter, and 3) a 1200nm long pass filter for each of the three gratings. The spectra taken with no long pass filter is most credible at the short wavelength side of the spectra, while the spectra taken with the 1200nm long pass filter is most credible at the longer wavelengths (Figure 34, Figure 35, and Figure 36). This is because the long pass filter removed light at low wavelengths that may be measured at double its wavelength due to second order diffraction.

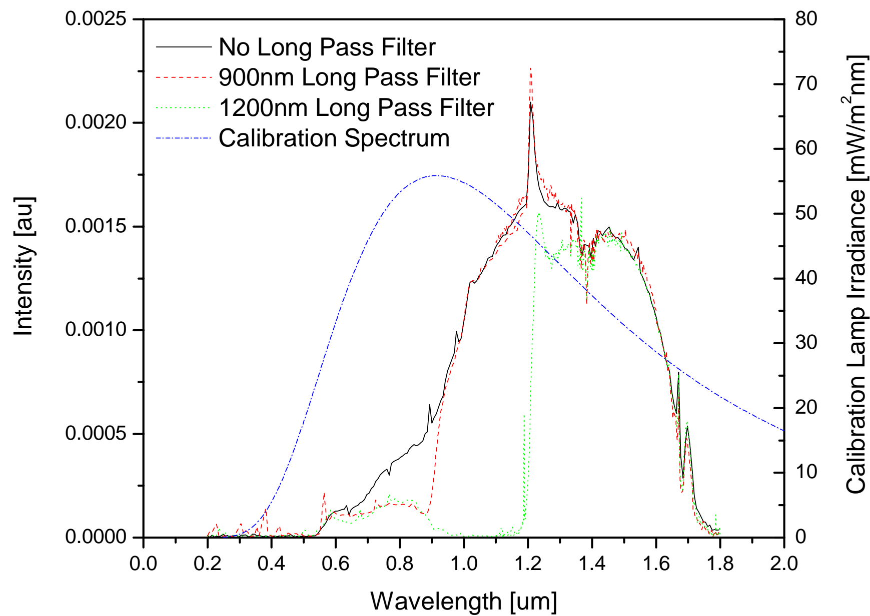

Figure 34: Spectra of calibration lamp using different long pass filter and a 300 line/mm 500nm blazed grating. This graph demonstrates how second order effects can be reduced by using long pass filters.

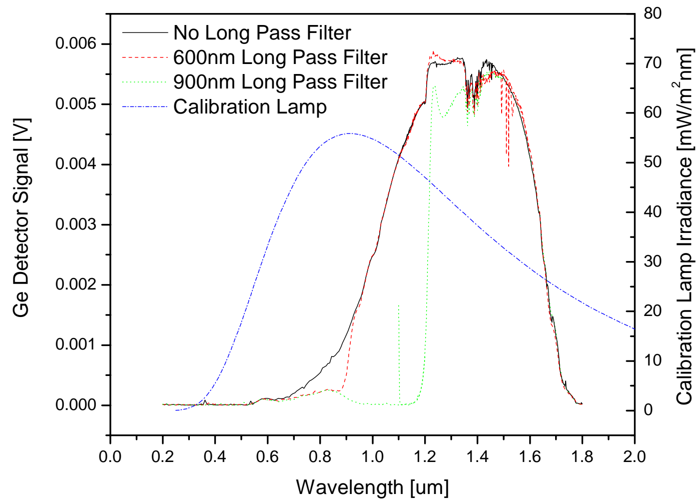

Figure 35: Spectra of calibration lamp using different long pass filter and a 300 line/mm 1000nm blazed grating. This graph demonstrates how second order effects can be reduced by using long pass filters.

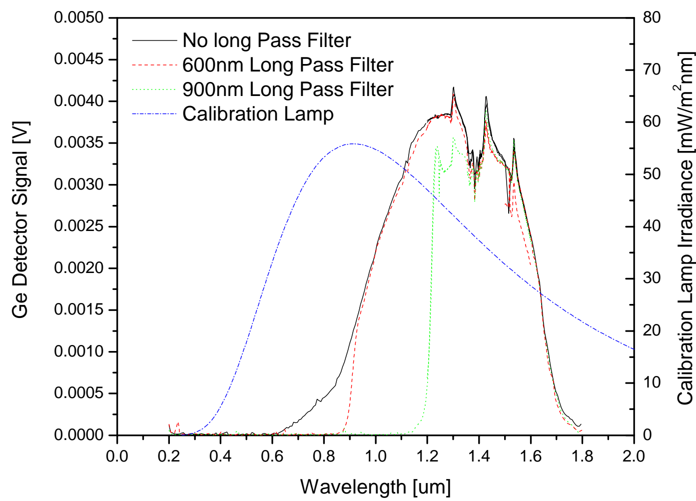

Figure 36: Spectra of calibration lamp using different long pass filter and a 150 line/mm 500nm blazed grating. This graph demonstrates how second order effects can be reduced by using long pass filters.

The agreement between the three scans indicates that second order light has little effect on the measured spectra.

The composite response spectra are made by scaling and splicing these three curves together where appropriate. The composite response spectrum of the calibration lamp is shown in Figure 37.

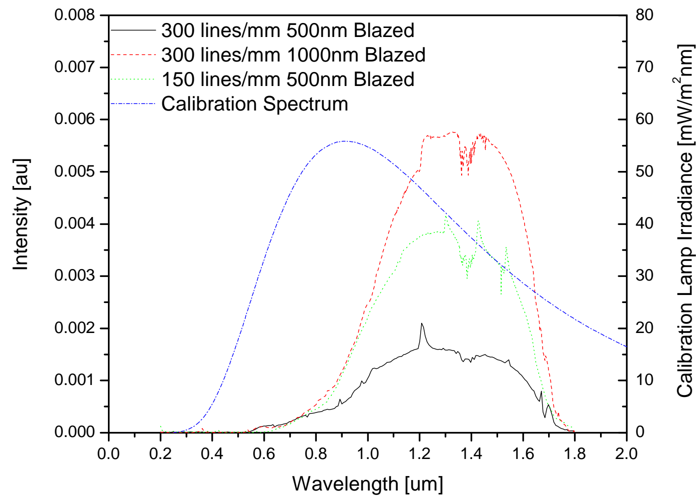

Figure 37: Spectra of the calibration lamp taken with three different gratings. The actual calibration spectrum is also plotted.

The response curve is then divided by the spectrum of the calibration lamp and normalized to find the response curve of the germanium detector and grating combination. The resulting calibration curve is shown below in Figure 38

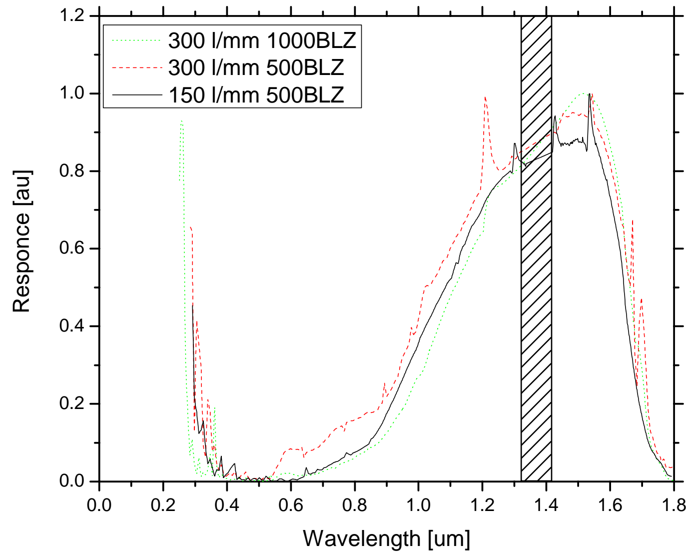

Figure 38: Response curve for the germanium detector using different grading.

The response feature shorter than 500nm occurs because the response function goes to zero at 250nm while there is still finite signal on the germanium detector (0.006 normalized units). This makes it difficult to resolve any spectral features below 500nm. Also one should note that in the shaded region around 1.4 μm is where water absorption occurs. The response of the detector is not accurate in this region. The best grating to use with the germanium detector is the 300 lines/mm 1000nm blazed.

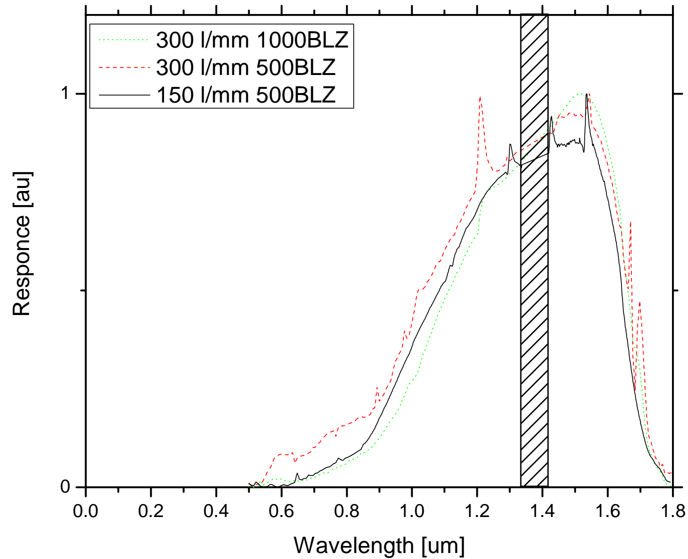

Figure 39: The final response curves for the germanium detector using the three available gratings.

Figure 39 shows the final response curve of for the germanium detector. To use this response curve, simply take the spectrum from the detector subtract the dark spectra and divide it by the response curve as shown below. This will result in the corrected spectra.

$$\text{Corrected Spectra} = \frac{\text{Raw spectra - Dark spectra}}{\text{System Responce}} \qquad 51$$

Calibration of the CCD Array Detector

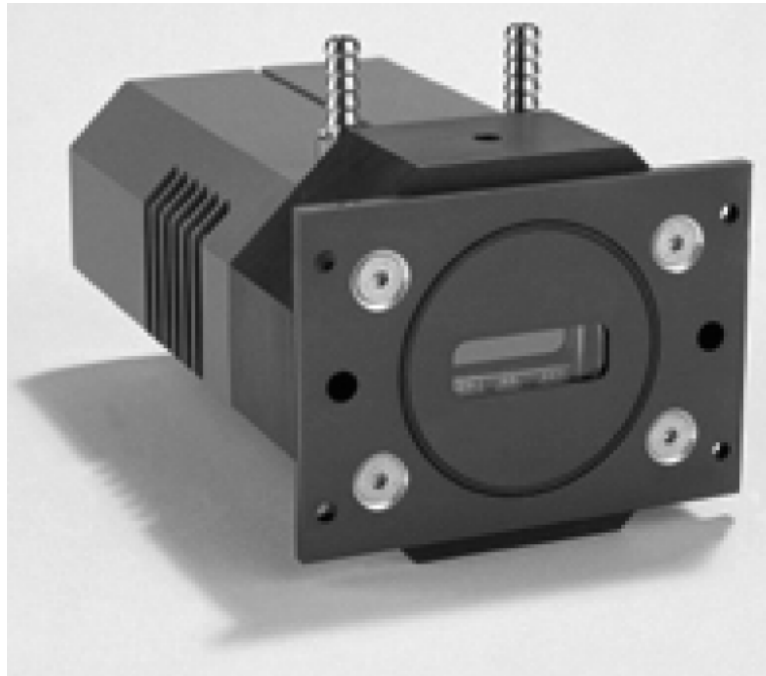

Figure 40: The Andor 20DU401-BR-DD CCD detector.

Calibration of a CCD array is somewhat more complex than that of a single element detector. Figure 41 shows a schematic diagram of the optical path for a Czerny-Turner grating monochromator and CCD array detector.

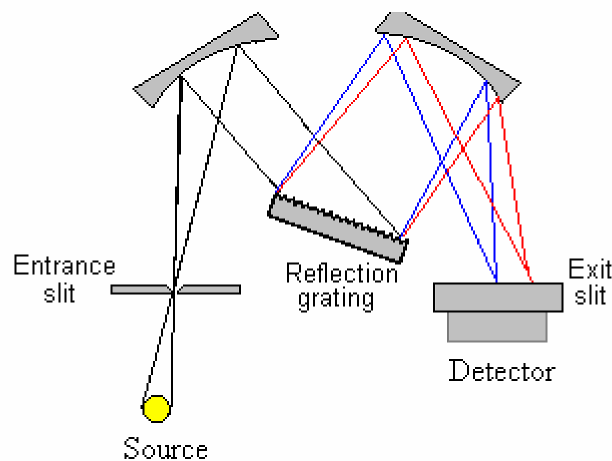

Figure 41: Czerny-Turner grating monochromator and CCD array.

In a CCD array configuration the constituent colors of light are separated and projected on different pixels of the CCD array. The CCD then returns an intensity map as a function of pixel number. The pixel number may be converted to wavelength since the grating angle and the relative pixel location is known.

The CCD array that is used in this calibration is the Andor 20DU401-BR-DD. The pixel array size is 1024 x 128. The response of the CCD is dominated by the silicon band gap. This band gap is 1.1eV and thus silicon may only absorb photons with energy greater than 1.1eV. The three gratings in the monochromator disperse the light such that one can only see a portion of the spectrum at a time. The two 300 lines/mm gratings allow for a view of the spectra spanning 278nm, and the 150 lines/mm will allow for a 565nm view of the spectra. Thus it will be necessary to take several spectra in order to cover the range from 250nm to 1300nm. This is shown below for the three gratings using no long pass filter (Figure 42, Figure 43, and Figure 44)

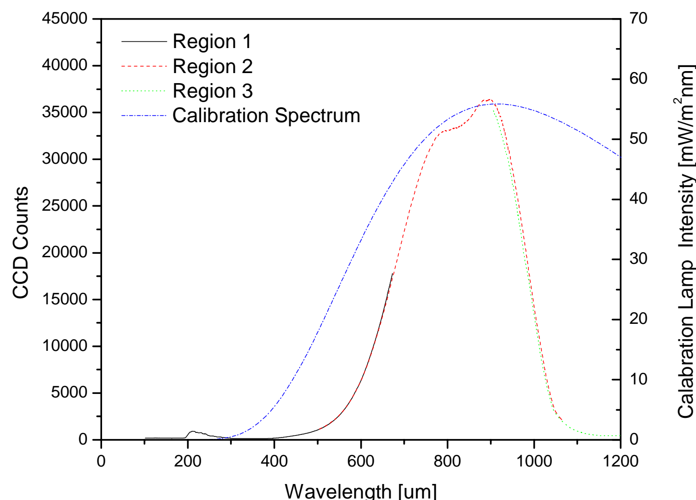

Figure 42: Spectra minus dark for the calibration source taken using the 150 l/mm 500nm blazed grating. Three spetra of diffrent regions are plotted together to cover the entire range. No long pass filter was used.

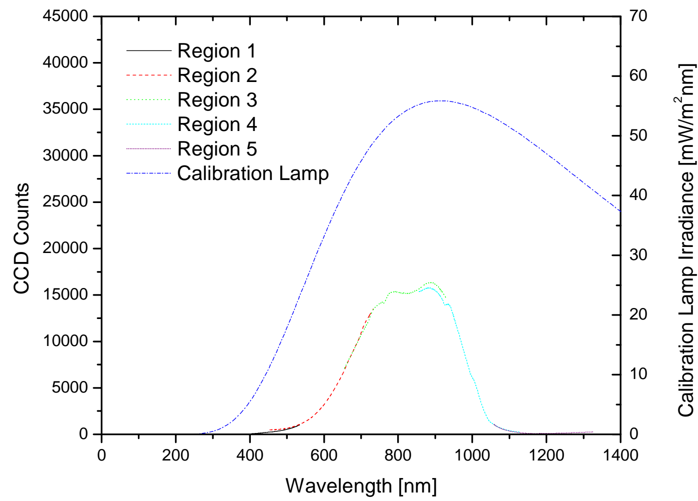

Figure 43: Spectra minus dark for the calibration source taken using the 300 l/mm 500nm blazed grating. Three spectra of different regions are plotted together to cover the entire range. No long pass filter was used.

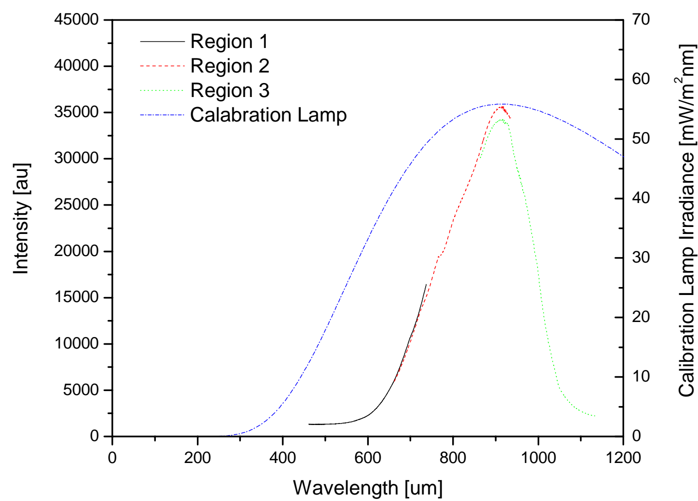

Figure 44: Spectra minus dark for the calibration source taken using the 300 l/mm 1000nm blazed grating. Three spectra of different regions are plotted together to cover the entire range. No long pass filter was used.

One can see from these graphs that the partial spectra do not fit perfectly together. This is attributed to the differences in pixels at different positions. It seems that the pixels on the small wavelength side of the spectrum return fewer counts for the same incident light than that of the pixels on the long wavelength side of the CCD. Attempts to correct for this effect were unsuccessful and thus this effect is not corrected in the current calibration.

Complete spectral curves across the useful range of the detector were formed by the above method with no long pass filter, a 600nm long pass filter, and a 900nm long pass filter. Spectra taken with a long pass filter will have smaller amplitude than spectra taken without a long pass filter. This was corrected for by scaling the spectra taken with the long pass filter to best match the spectra taken without the long pass filter. Figure 45, Figure 46, and Figure 47 show the scaled spectra taken with each of the long pass filters using different gratings.

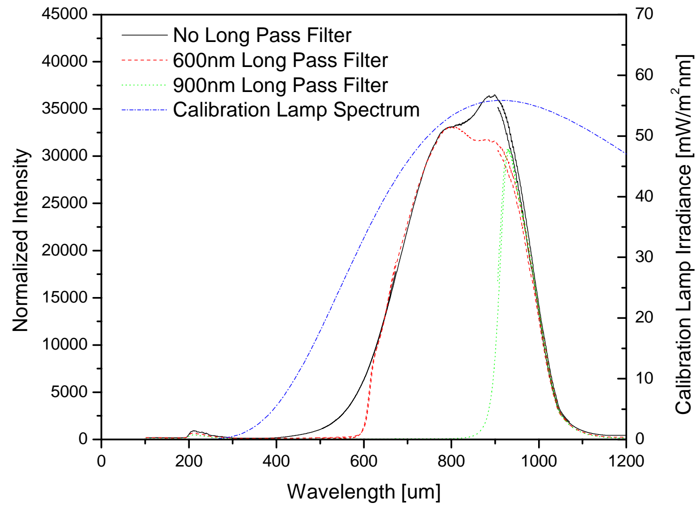

Figure 45: Spectra of the calibration source using 150 l/mm 500nm blazed grating and different long pass filters to get an accurate representation of the spectrum.

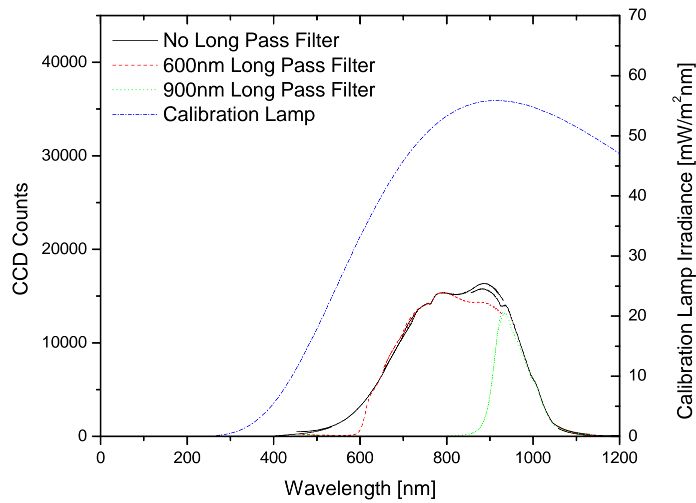

Figure 46: Spectra of the calibration source using 300 l/mm 500nm blazed grating and different long pass filters to get an accurate representation of the spectrum.

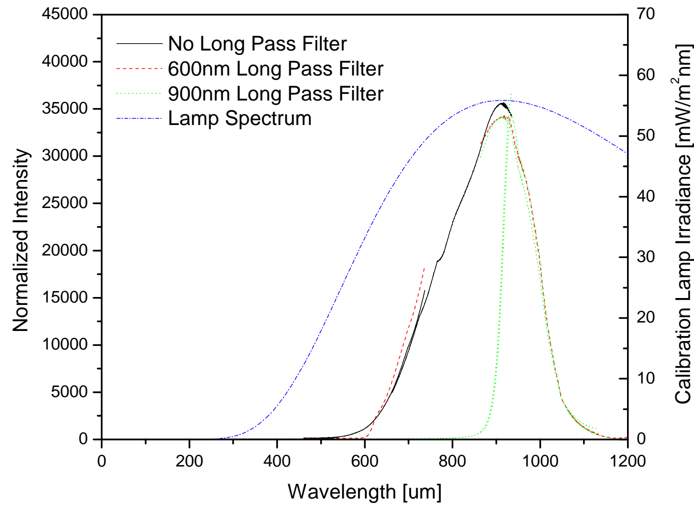

Figure 47: Spectra of the calibration source using 300 l/mm 1000nm blazed grating and different long pass filters to get an accurate representation of the spectrum.

A composite spectrum of the source for each grating can be created by combining the three spectra for each grating. At low wavelengths the spectra taken with no long pass filter will be most accurate, while above about 650nm the spectra taken with the 600nm long pass filter will be most accurate and the spectra taken with the 900nm long pass filter will be most accurate above about 950nm. The composite spectrum is made by using those portions of each spectrum where appropriate and splicing them all together. When splicing these spectra together the spectra were cut where the data was crossing or close together. In the event that the data did not cross the data was cut leaving a gap between the two datasets. Then the data was fit with a polynomial to fill the gap in the data (Figure 48, Figure 49, Figure 50, and Figure 51)

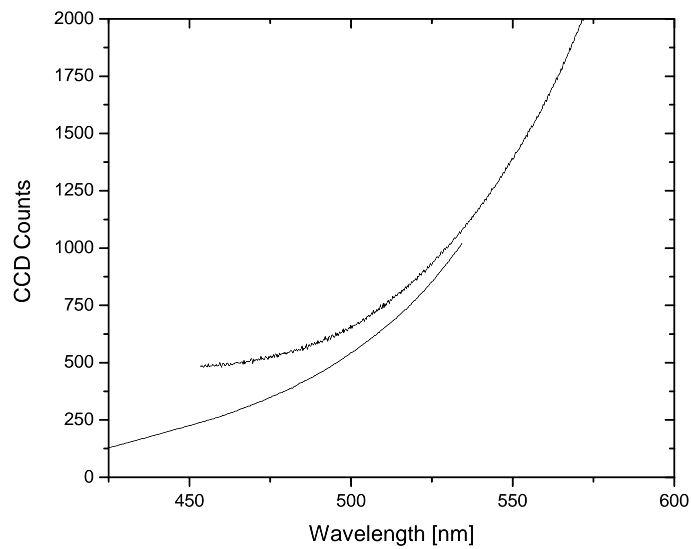

Figure 48: Spectra that do not overlap.

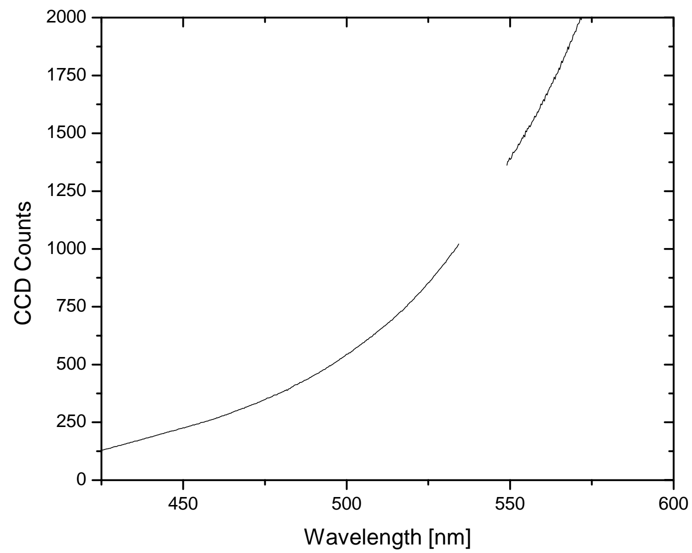

Figure 49: Cut spectra such that there is a small gap between the tow data sets. Place both data sets together in a third data set.

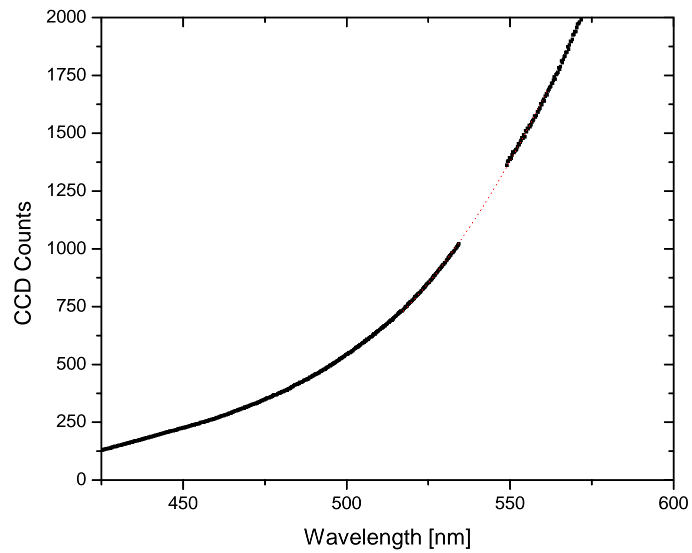

Figure 50: Fit with a polynomial of appropriate order.

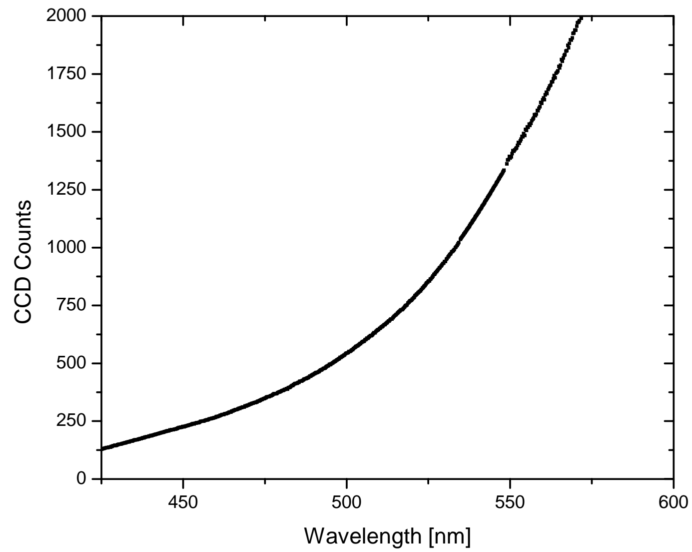

Figure 51: Splice the polynomial data into the third data set.

The resulting composite spectra for each CCD grating combination are shown in Figure 52.

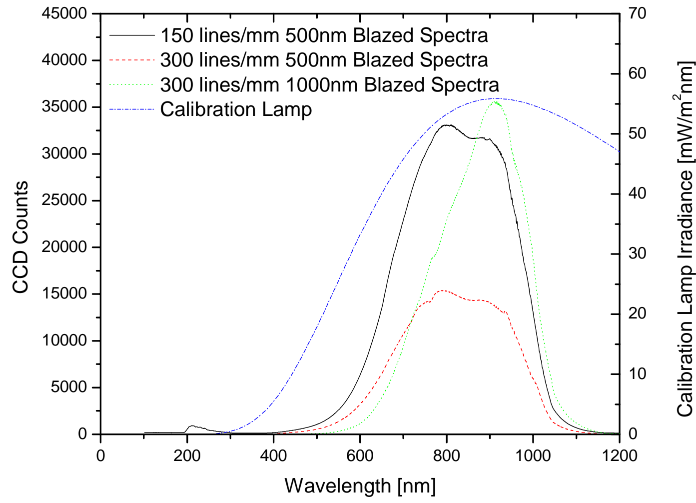

Figure 52: The spectra of the calibration lamp taken with the three different gratings and the CCD detector. The actual spectra of the calibration lamp is also plotted.

These composite spectra are then divided by the known spectra of the calibration lamp to give the response of the grating CCD combination. This data is presented for each grating CCD combination in Figure 53.

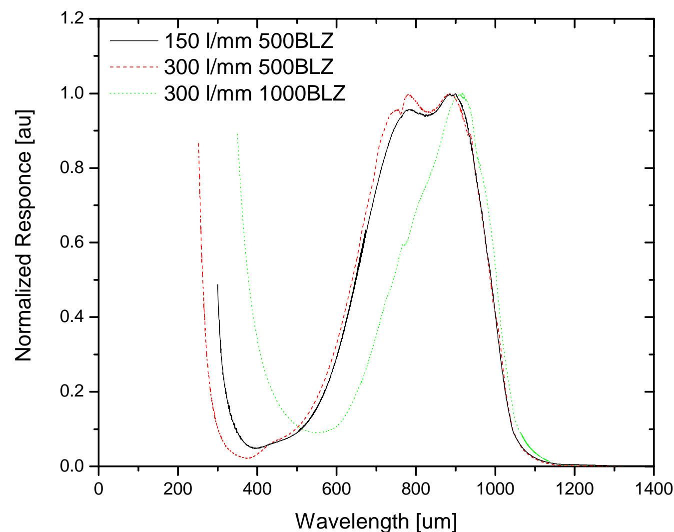

Figure 53: Response curve for the CCD array using different gratings.

At the low wavelength range the response blows up because of an offset of the measured spectral data. Thus the measured spectrum is finite when the known analytical lamp spectrum goes to zero at 250nm. The division of the measured data by the lamp data thus produces this artifact. For our purposes we will crop this artifact off of the response curve. Better data should be taken in this range if data is to be analyzed in this region. Figure 54 shows the cropped response data.

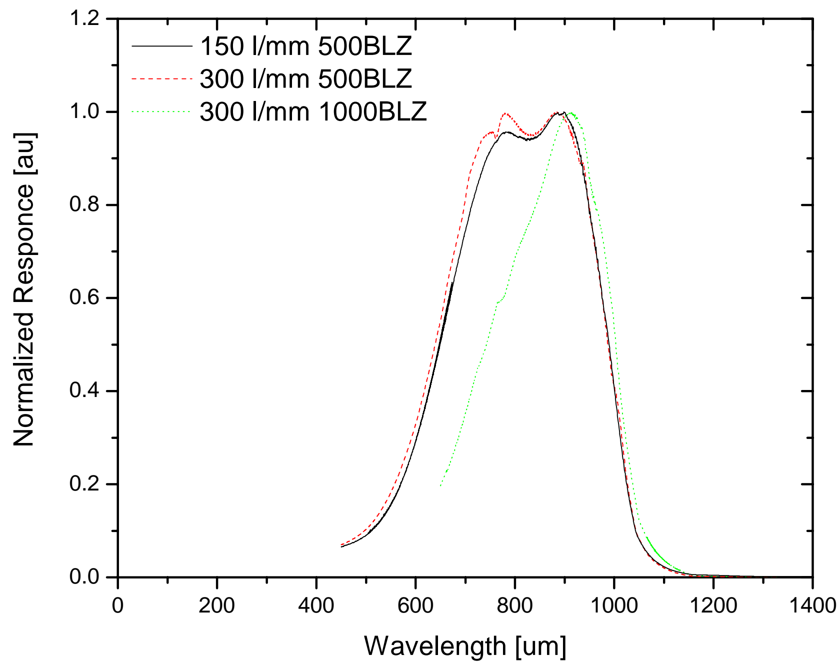

Figure 54: Response spectra after being cropped to the useable range.

To use this response curve, simply take the spectrum from the detector subtract the dark spectra and divide it by the response curve. This will result in the corrected spectra.

$$\text{Corrected Spectra} = \frac{\text{Raw spectra - Dark spectra}}{\text{System Responce}} \tag{52}$$

APPENDIX B: RESULTS OF RBS EXPERIMENTS

In this section the energy histograms and resulting fits obtained by using RUMP are presented to show the composition of each sample used in this study.

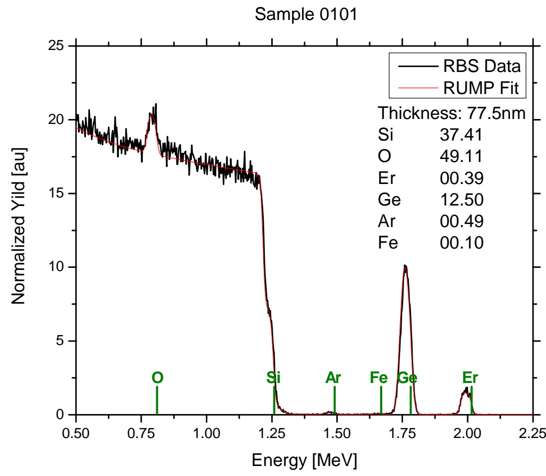

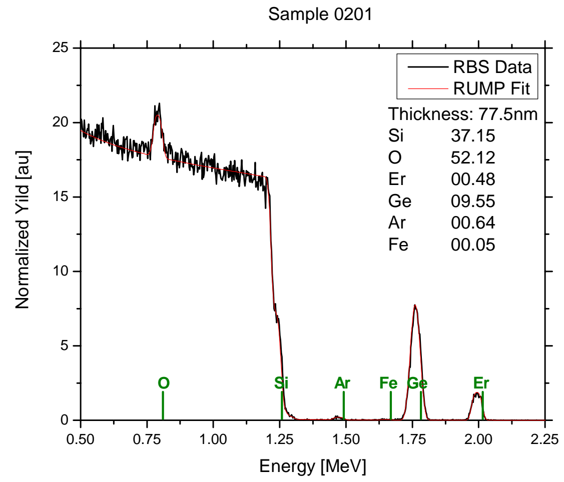

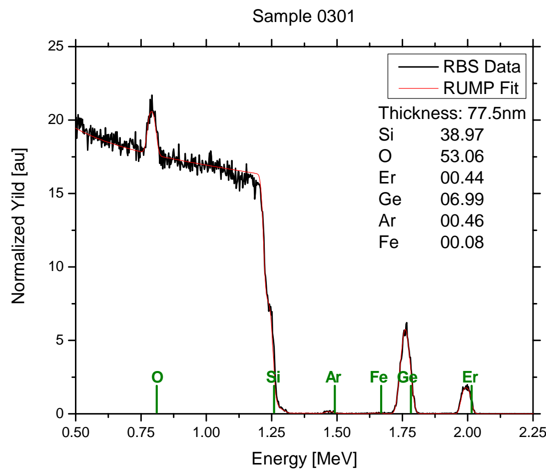

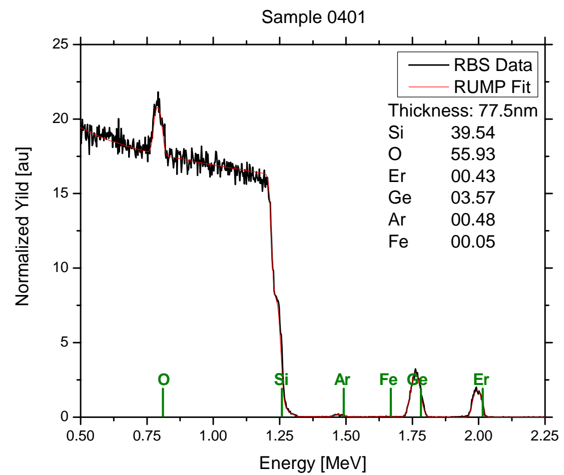

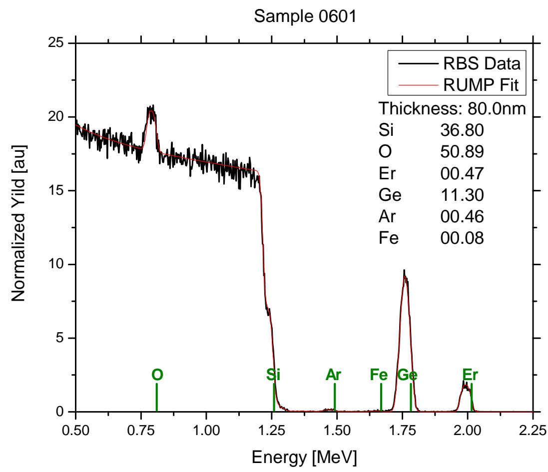
Sample 0601
RBS Data
RUMP Fit
Thickness: 80.0nm
Si 36.80
O 50.89
Er 00.47
Ge 11.30
Ar 00.46
Fe 00.08
Normalized Yild [au]
Energy [MeV]
O
Si
Ar
Fe
Ge
Er

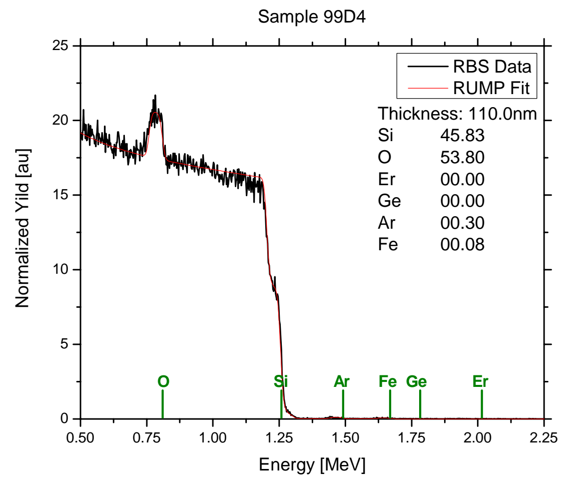
Sample 99D4
RBS Data
RUMP Fit
Thickness: 110.0nm
Si 45.83
O 53.80
Er 00.00
Ge 00.00
Ar 00.30
Fe 00.08
Normalized Yild [au]
Energy [MeV]
O
Si
Ar
Fe
Ge
Er

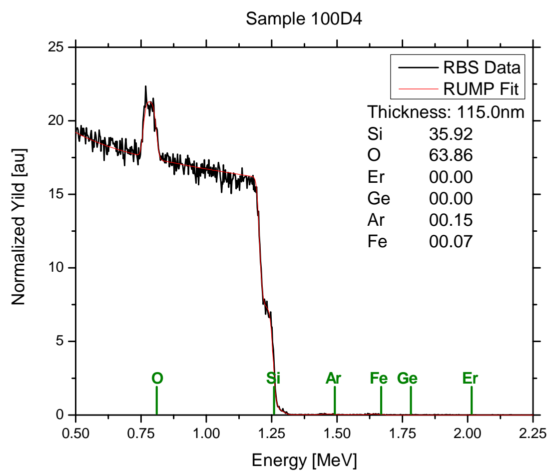
Sample 100D4
RBS Data
RUMP Fit
Thickness: 115.0nm
Si 35.92
O 63.86
Er 00.00
Ge 00.00
Ar 00.15
Fe 00.07
Normalized Yild [au]
Energy [MeV]
O
Si
Ar
Fe
Ge
Er

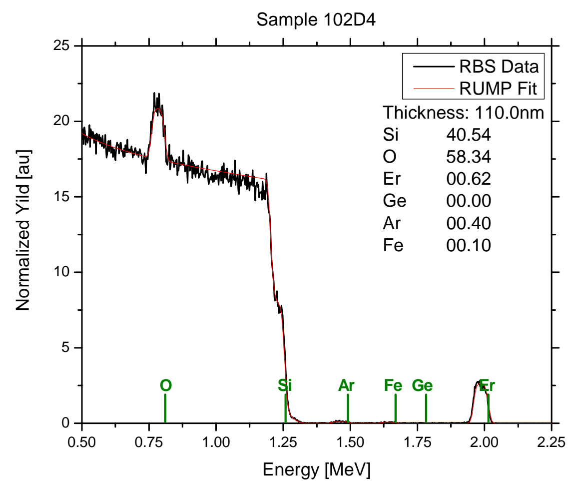
Sample 102D4
RBS Data
RUMP Fit
Thickness: 110.0nm
Si 40.54
O 58.34
Er 00.62
Ge 00.00
Ar 00.40
Fe 00.10
Normalized Yild [au]
Energy [MeV]
O
Si
Ar
Fe
Ge
Er

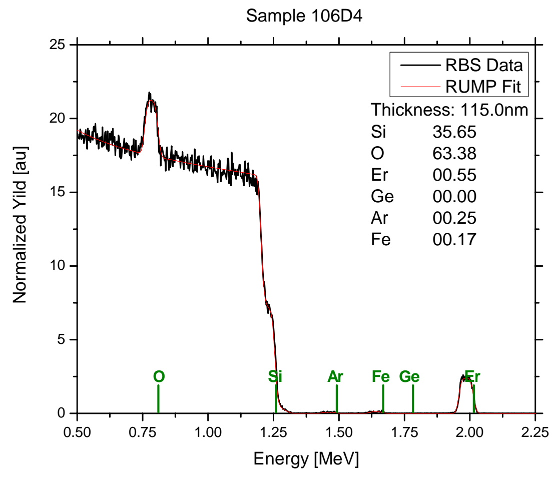
Sample 106D4
RBS Data
RUMP Fit
Thickness: 115.0nm
Si 35.65
O 63.38
Er 00.55
Ge 00.00
Ar 00.25
Fe 00.17
Normalized Yild [au]
Energy [MeV]
O
Si
Ar
Fe
Ge
Er
0
5
10
15
20
25
0.50
0.75
1.00
1.25
1.50
1.75
2.00
2.25

APPENDIX C: DERIVATION OF THE EFFECTIVE Er EXCITATION CROSS SECTION

In this section the effective Er related cross section is derived from the quasi two level system achieved in Section 2.1. The rate equation that describes the excited state population in the quasi two level system is shown in Equation 13.

$$\frac{dN_1}{dt} = R_{02}N_0 - R_{10}N_1 \tag{53}$$

The total population of atoms is constant so Equation 54 also applies to this system.

$$N_T = N_0 + N_1 \tag{54}$$

Equation 54 can be solved for N_0 and substituted in to Equation 13 in order to achieve Equation 55.

$$\frac{dN_1}{dt} = R_{02}N_T - (R_{10} + R_{02})N_1 \tag{55}$$

Equation 55 has a solution of the form of Equation 56.

$$N_1 = A + Be^{-t/\tau} \tag{56}$$

By substitution of Equation 56 in to Equation 55, Equation 57 is found.

$$-\frac{B}{\tau}e^{-t/\tau} = R_{02}N_T - A(R_{10}+R_{02}) - B(R_{10}+R_{02})e^{-t/\tau} \qquad 57$$

It can be observed that the first two terms on the right hand side of Equation 57 must sum to zero. Thus the constant *A* is achieved (Equation 58).

$$A = \frac{R_{02}N_T}{(R_{10}+R_{02})} \qquad 58$$

This leaves Equation 59.

$$-\frac{B}{\tau}e^{-t/\tau} = -B(R_{10}+R_{02})e^{-t/\tau} \qquad 59$$

Equation can be solved for $1/\tau$ (Equation 60).

$$\frac{1}{\tau} = R_{10} + R_{02} \qquad 60$$

By making a measurement of the rise time of the emission at 1.535μm and fitting that rise time measurement the value for $1/\tau$ can be found. Similarly a fit of the decay time results in the value for $R_{10}=1/\tau_{10}$. R_{02} is related to the pump flux by the effective Er cross section ($R_{02}=\sigma\varphi$). Making these observations and substituting into Equation 60 it is observed that the effective Er cross section is given by Equation 49.

$$\sigma_{sens} \propto \frac{1}{\tau_{Up,i}} - \frac{1}{\tau_{Dn,i}} \qquad 61$$

LIST OF REFERENCES

1. Kenyon, A.J., et al., *Luminescence from erbium-doped silicon nanocrystals in silica: Excitation mechanisms.* Journal of Applied Physics, 2002. **91**(1): p. 367-374.

2. Paniccia, M., V. Krutul, and S. Koehl, *Intel Unveils Silicon Photonics Breakthrough: High-Speed Silicon Modulation*, in *Technology@Intel Magazine*. 2004. p. 1.

3. Paniccia, M., V. Krutul, and S. Koehl, *Introducing Intel's Advances in Silicon Photonics*, in *White Paper*. 2004.

4. Lee, K.K., et al., *Effect of size and roughness on light transmission in a Si/SiO_2 waveguide: Experiments and model.* Applied Physics Letters, 2000. **77**(11): p. 1617-1619.

5. Salib, M., et al., *Silicon Photonics.* Intel Technology Journal, 2004. **8**(2): p. 20.

6. Gun, C., *CMOS Photonics for High-Speed Interconnects.* IEEE Computer Society, 2006. **6**: p. 58.

7. Fox, M., *Optical Properties of Solids*. 2001, New York: Oxford University Press.

8. Gardelis, S., et al., *Evidence for quantum confinement in the photoluminescence of porous Si and SiGe.* Applied Physics Letters, 1991. **59**(17): p. 2118-2120.

9. Canham, L.T., *Silicon quantum wire array fabrication by electrochemical and chemical dissolution of wafers.* Applied Physics Letters, 1990. **57**(10): p. 1046-1048.

10. van den Hoven, G.N., et al., *Upconversion in Er-implanted Al_2O_3 waveguides.* Journal of Applied Physics, 1996. **79**(3): p. 1258.

11. Kik, P.G., M.L. Brongersma, and A. Polman, *Strong exciton-erbium coupling in Si nanocrystal-doped SiO_2.* Applied Physics Letters, 2000. **76**(17): p. 2325.

12. Priolo, F., et al., *Excitation and non-radiative de-excitation processes in Er-doped Si nanocrystals.* Materials Science and Engineering B, 2001. **81**(1-3): p. 9.

13. Fujii, M., et al., *1.54 mu m photoluminescence of Er^{3+} doped into SiO_2 films containing Si nanocrystals: Evidence for energy transfer from Si nanocrystals to Er^{3+}*. Applied Physics Letters, 1997. **71**(9): p. 1198-1200.

14. Fujii, M., et al., *Photoluminescence from SiO_2 films containing Si nanocrystals and Er: Effects of nanocrystalline size on the photoluminescence efficiency of Er^{3+}*. Journal of Applied Physics, 1998. **84**(8): p. 4525-4531.

15. Franzo, G., V. Vinciguerra, and F. Priolo, *The excitation mechanism of rare-earth ions in silicon nanocrystals.* Applied Physics A: Materials Science & Processing, 1999. **69**(1): p. 3.

16. Gaponenko, S.V., *Optical Properties of Semiconductor Nanocrystals*. 1998, New Yourk: Cambridge University Press.

17. Kimiaki, T., et al., *Effects of P doping on photoluminescence of* $Si_{1-x}Ge_x$ *alloy nanocrystals embedded in* SiO_2 *matrices: Improvement and degradation of luminescence efficiency.* Journal of Applied Physics, 2001. **90**(10): p. 5147-5151.

18. C. Delerue, M.L.G.A., *Tight Binding for Complex Semiconductor Systems.* physica status solidi (b), 2001. **227**(1): p. 115-149.

19. Biteen, J.S., et al., *Size-dependent oxygen-related electronic states in silicon nanocrystals.* Applied Physics Letters, 2004. **84**(26): p. 5389.

20. Kayanuma, Y., *Wannier exciton in microcrystals.* Solid State Communications, 1986. **59**(6): p. 405.

21. Timoshenko, V.Y., et al., *Comparative study of photoluminescence of undoped and erbium-doped size-controlled nanocrystalline Si/*SiO_2 *multilayered structures.* Journal of Applied Physics, 2004. **96**(4): p. 2254-2260.

22. Weber, J. and M.I. Alonso, *Near-band-gap photoluminescence of Si-Ge alloys.* Physical Review B, 1989. **40**(8): p. 5683.

23. Watanabe, Y., et al., *Formation and Properties of Porous Silicon and Its Application.* Journal of The Electrochemical Society, 1975. **122**(10): p. 1351.

24. Elhouichet, H., et al., *Changes in photoluminescence behavior and structure of porous silicon related to preparation conditions and laser irradiation.* Thin Solid Films, 1997. **304**(1-2): p. 358.

25. Bording, J.K. and J. TaftÃ¸, *Molecular-dynamics simulation of growth of nanocrystals in an amorphous matrix.* Physical Review B, 2000. **62**(12): p. 8098.

26. Riabinina, D., et al., *Nucleation and growth of Si nanocrystals in an amorphous* SiO_2 *matrix.* Physical Review B (Condensed Matter and Materials Physics), 2006. **74**(7): p. 075334.

27. Johnson, N.M., D.K. Biegelsen, and M.D. Moyer, *Low-temperature annealing and hydrogenation of defects at the Si-*SiO_2 *interface.* Journal of Vacuum Science and Technology, 1981. **19**(3): p. 390-395.

28. Brongersma, M.L., et al., *Size-dependent electron-hole exchange interaction in Si nanocrystals.* Applied Physics Letters, 2000. **76**(3): p. 351.

29. Imakita, K., M. Fujii, and S. Hayashi, *Spectrally resolved energy transfer from excitons in Si nanocrystals to Er ions.* Physical Review B, 2005. **71**(19).

30. Kik, P.G., et al., *Excitation and deexcitation of Er^{3+} in crystalline silicon.* Applied Physics Letters, 1997. **70**(13): p. 1721.

31. Kik, P.G., *Energy transfer in erbium doped optical waveguides based on silicon*. 2000, FOM-Institute for Atomic and Molecular Physics: Amsterdam. p. 120.

32. Franzo, G., et al., *Er^{3+} ions--Si nanocrystals interactions and their effects on the luminescence properties.* Applied Physics Letters, 2000. **76**(16): p. 2167.

33. Watanabe, K., M. Fujii, and S. Hayashi, *Resonant excitation of Er^{3+} by the energy transfer from Si nanocrystals.* Journal of Applied Physics, 2001. **90**(9): p. 4761-4767.

34. Imakita, K., M. Fujii, and S. Hayashi, *The mechanism of energy transfer from Si nanocrystals to Er ions in SiO_2.* The European Physical Journal D - Atomic, Molecular and Optical Physics, 2005. **34**(1 - 3): p. 161.

35. Yang, Y.M., et al., *Formation, structure, and phonon confinement effect of nanocrystalline $Si_{1-x}Ge_x$ in SiO_2-Si-Ge cosputtered films.* Journal of Applied Physics, 2004. **96**(9): p. 5239.

36. Craciun, V., et al., *Low temperature UV oxidation of SiGe for preparation of Ge nanocrystals in SiO_2.* Thin Solid Films, 1995. **255**(1-2): p. 290.

37. Schoisswohl, M., et al., *Structure and visible photoluminescence of porous $Si_{1-x}Ge_x$.* Physical Review B (Condensed Matter), 1995. **52**(16): p. 11898-11903.

38. Takeoka, S., et al., *Control of photoluminescence energy of Si nanocrystals by Ge doping.* Journal of Luminescence, 2000. **87-89**: p. 350.

39. Fujii, M., et al., *Breakdown of the k-conservation rule in $Si_{1-x}Ge_x$ alloy nanocrystals: Resonant photoluminescence study.* Journal of Applied Physics, 2000. **88**(10): p. 5772-5776.

40. Kimiaki, T., et al., *Electron spin resonance study of defects in $Si_{1-x}Ge_x$ alloy nanocrystals embedded in SiO_2 matrices: Mechanism of luminescence quenching.* Journal of Applied Physics, 2001. **89**(9): p. 4917-4920.

41. Polman, A., et al., *Erbium In Crystal Silicon - Optical Activation, Excitation, And Concentration Limits.* Journal Of Applied Physics, 1995. **77**(3): p. 1256-1262.

42. Quimby, R.S., W.J. Miniscalco, and B. Thompson, *Clustering in erbium-doped silica glass fibers analyzed using 980 nm excited-state absorption.* Journal of Applied Physics, 1994. **76**(8): p. 4472-4478.